INTERNATIONAL JOURNAL FOR NUMERICAL METHODS IN FLUIDS
Int. J. Numer. Meth. Fluids 2006; **50**:27–61
Published online 30 September 2005 in Wiley InterScience (www.interscience.wiley.com). DOI: 10.1002/fld.1023

Large eddy simulation (2D) of spatially developing mixing layer using vortex-in-cell for flow field and filtered probability density function for scalar field

J. K. Wang and R. E. Milane*,†

Department of Mechanical Engineering, University of Ottawa, 161 Louis Pasteur, Ottawa, Ont., Canada K1N 6N5

SUMMARY

A large eddy simulation based on filtered vorticity transport equation has been coupled with filtered probability density function transport equation for scalar field, to predict the velocity and passive scalar fields. The filtered vorticity transport has been formulated using diffusion-velocity method and then solved using the vortex method. The methodology has been tested on a spatially growing mixing layer using the two-dimensional vortex-in-cell method in conjunction with both Smagorinsky and dynamic eddy viscosity subgrid scale models for an anisotropic flow. The transport equation for filtered probability density function is solved using the Lagrangian Monte-Carlo method. The unresolved subgrid scale convective term in filtered density function transport is modelled using the gradient diffusion model. The unresolved subgrid scale mixing term is modelled using the modified Curl model. The effects of subgrid scale models on the vorticity contours, mean streamwise velocity profiles, root-mean-square velocity and vorticity fluctuations profiles and negative cross-stream correlations are discussed. Also the characteristics of the passive scalar, i.e. mean concentration profiles, root-mean-square concentration fluctuations profiles and filtered probability density function are presented and compared with previous experimental and numerical works. The sensitivity of the results to the Schmidt number, constant in mixing frequency and inflow boundary conditions are discussed. Copyright © 2005 John Wiley & Sons, Ltd.

KEY WORDS: large eddy simulation; diffusion-velocity method; vortex-in-cell; Smagorinsky; dynamic eddy viscosity; filtered probability density function; mixing layer

1. INTRODUCTION

Numerically, the techniques used in the simulation of shearing flows can be categorized into Eulerian methods and Lagrangian methods. In Eulerian methods, such as finite difference and

*Correspondence to: R. E. Milane, Department of Mechanical Engineering, University of Ottawa, 161 Louis Pasteur, Ottawa, Ont., Canada K1N 6N5.
†E-mail: milane@eng.uottawa.ca

Contract/grant sponsor: National Sciences and Engineering Research Council

Received 5 October 2004
Revised 10 May 2005
Accepted 12 May 2005

finite element methods, computational requirements are affordable but these methods entail numerical dissipation. Lagrangian methods such as vortex methods, are immune from numerical dissipation but are computationally expensive. The vortex-in-cell (VIC) method combines the best features of Eulerian methods and Lagrangian methods. In VIC, Eulerian method is used to calculate the velocity field and Lagrangian method is used to track the vortices by using an interpolation scheme to transfer vorticity and velocity between the nodes of the grid and the vortices. The numerical dissipation in VIC comes from the interpolation scheme and from the Eulerian method used to calculate the velocity field. However the overall numerical diffusion in VIC is reduced relative to the Eulerian methods [1–4]. This is done at the expense of the computational requirements (CPU and memory) that are more expensive than the Eulerian method (such as finite difference) but are reduced relative to the pure Lagrangian method. Cottet and Koumoutsakos [5] discussed clearly the advantages and disadvantages of the VIC and finite-difference. In VIC, the vorticity transport is handled exactly by following the trajectories of vortex elements whereas finite difference assumes that the solution is represented by a polynomial. Therefore, VIC is more robust. Furthermore, the solution of the convection part of VIC does not require a time step governed by a CFL condition as in an explicit finite difference scheme. However Eulerian methods (such as finite-difference) are more flexible when a viscous boundary condition such as flow around obstacles is calculated. In this case the Eulerian–Lagrangian domain decomposition technique is used where the Eulerian method is used around obstacles and a pure Lagrangian method between obstacles.

Vortex methods have been applied to various flow configurations [4]. In particular, numerous studies simulating two-dimensional temporal and spatially growing mixing layers have been carried out. The Lagrangian technique was used in the simulation of the spatially growing unforced mixing layer by Ashurst [6], Kuwahara and Takami [7], Ghoniem and Ng [8], Inoue and Leonard [9], and to the forced mixing layer by Ghoniem and Ng [10], Inoue and Leonard [9] and Inoue [11]. Aref and Siggia [12] used the VIC to simulate a temporal mixing layer and Abdolhosseini and Milane [13] extended the VIC to a spatially growing mixing layer. Generally, these studies showed that the roll-up of pair of lumps is the primary growth mechanism of mixing layers and is responsible for the entrainment of the surrounding non-turbulent fluid.

In recent works, the Lagrangian vortex method has been developed in the context of large eddy simulation (LES) by filtering the vorticity transport equation and modelling the subgrid scale (SGS) velocity and vorticity fluctuations using the eddy viscosity SGS model [14]. Both Smagorinsky and dynamic eddy viscosity SGS models were implemented and constants in both SGS models were obtained specifically for the vorticity equation. In the Lagrangian representation, the effect of eddy viscosity model was implemented by modifying the strength of the particles using the particle strength exchange (PSE) [15]. Other LES based on core-spreading, valid in the limit of vanishing viscosity [5, 16], have been used by Milane and Nourazar [17, 18]. Cottet [19] presented SGS model based on a rigorous analysis of truncation error of the filtered vorticity transport and developed a scheme based on the PSE method for small-scale contribution.

The diffusion-velocity method is an alternative way for simulating the diffusion equation and can be extended to an eddy-viscosity-based LES formulation. Originally, Ogami and Akamatsu [20] introduced the method as an alternative to the random walk solution of the diffusion equation in order to extend the solution to Reynolds number values, below the lower limit of applicability of the random walk. The method was used by Clarke and Tutty [21]

in predicting various flows past circular cylinders. Recently, Milane [22] has developed a LES based on diffusion-velocity method for the vorticity transport using Smagorinsky eddy viscosity SGS model.

In several investigations by Ghoniem and Givi [3], Ghoniem and Heidarinejad [23] and Knio and Ghoniem [24], a sheared layer was simulated using the vortex method to solve the vorticity transport and the scalar element method to solve the scalar transport. Both the vortex method and the scalar element method are based on the discretization of the vorticity and the scalar gradients into elements which are transported along particle paths. An alternative method widely used to simulate the scalar field in turbulent flows is based on the solution of the transport equation for probability density function (PDF) of scalar. Pope [25–27] has developed transport equations for PDFs which were solved using the Monte-Carlo technique. The main advantage of PDF method is that chemical reaction is treated without approximation, besides the fact that the PDFs yield all the statistical information regarding the scalar field. Gao and O'Brien [28] introduced the transport equation for the large eddy PDF (LEPDF) for a chemically reacting flow. Also Colucci *et al*. [29] developed LES based on PDF, termed the filtered density function (FDF) for a chemically reacting turbulent flow field. The reacting field was obtained from the solution of the filtered Navier–Stokes equation and the FDF transport. The unresolved subgrid convective term in the FDF transport is modelled using the gradient diffusion model. The methodology was assessed using a temporal mixing layer and a spatially developing planar jet. Jaberi *et al.* [30] developed a methodology named 'filtered mass density function' (FMDF) by extending the work of Colucci *et al*. [29] to variable density and reacting flows at low Mach numbers. Zhou and Pereira [31] implemented the FDF methodology developed by Colucci *et al.* [29] to investigate the two-dimensional, spatially developing, reacting and non-reacting, constant-density, mixing layer in a flow regime prior to the mixing transition similar to the experiment of Masutani and Bowman [32]. The FDF results showed satisfactory agreement with experimental measurements.

Experimentally, Konrad [33] studied the extent of passive scalar mixing in a gaseous mixing layer with a velocity ratio $r = 0.3$ (ratio of low-to-high velocity). In the pre-mixing transition region, the PDFs are non-marching, i.e. the most probable concentration is the same across the mixing layer and is biased toward the high-speed side. Batt [34] investigated experimentally scalar mixing in a gaseous mixing layer with $r = 0.08$. The PDFs showed marching behaviour across the mixing layer, i.e. the most probable concentration varies across the layer, with the most probable value on each side of the layer being closer to the free stream value of that side. Also the root-mean-square (rms) scalar fluctuations showed a bimodal behaviour, i.e. a dip in the rms profile, with an asymmetry in the profile. Masutani and Bowman (M and B) [32] examined the structure of scalar field in gaseous mixing layer with $r = 0.5$, in the pre-mixing transition region. The PDFs were non-marching across the mixing layer similar to the results of Konrad [33]. Recently, Pickett and Ghandhi [35] reported results for $r = 0.2, 0.3$ and 0.4, in gaseous mixing layers. Their study suggested that non-marching PDFs produces a triple inflection point in the mean concentration profiles, whereas marching PDFs produce a single inflection point, as pointed out in the earlier study of Clemens and Mungal [36].

The purpose of this study is to extend the LES, based on the filtered vorticity transport which was formulated using the diffusion-velocity method in Reference [22], by including a dynamic SGS model and the FDF transport for passive scalar to predict the velocity and scalar fields. The methodology will be tested on a spatially developing mixing layer. The

filtered vorticity transport is solved using VIC inconjunction with both the Smagorinsky and dynamic eddy viscosity SGS models. The FDF transport equation for scalar is solved using the Lagrangian Monte-Carlo method. The subgrid convective term is modelled using the gradient diffusion model and the mixing is modelled using the modified Curl model. Comparison is made with two-dimensional experimental results of Masutani and Bowman [32] and numerical simulation of Zhou and Pereira [31]. The mean velocity, the rms velocity fluctuations and negative velocity cross-correlation, mean scalar concentrations, rms scalar fluctuations and FDFs are presented. The effect of Schmidt number, constant in mixing frequency and inflow boundary conditions on scalar field is discussed.

2. VORTEX-IN-CELL

2.1. Vorticity equation

The continuity and vorticity transport equations for an incompressible flow and viscous fluid are, respectively,

$$\frac{\partial u_i}{\partial x_i} = 0 \tag{1}$$

$$\left\{\frac{\partial \omega_i}{\partial t}\right\} + u_j \frac{\partial \omega_i}{\partial x_j} = \omega_j \frac{\partial u_i}{\partial x_j} + \nu \frac{\partial^2 \omega_i}{\partial x_j \partial x_j} \tag{2}$$

where ω_i represents the component of the vorticity vector ω, u_i and u_j represent the components of the velocity vector $\mathbf{u}$, and ν is the kinematic viscosity. The left-hand side of Equation (2) includes the rate of change of vorticity in time and due to convection, respectively. The first term on the right-hand side is the vortex stretching term, and the second term on the right-hand side is the viscous diffusion.

For a 2D flow parallel to (x, y) plane, the velocity vector is $\mathbf{u} = \mathbf{u}(x, y, t)$, the vorticity vector ω_z reduces to one component in the z direction, perpendicular to the (x, y) plane, and the stretching term vanishes. Therefore Equation (2) reduces to

$$\frac{\partial \omega_z}{\partial t} + u_j \frac{\partial \omega_z}{\partial x_j} = \nu \frac{\partial^2 \omega_z}{\partial x_j \partial x_j} \tag{3}$$

A different form of vorticity equation can be written if the continuity (Equation (1)) is combined with the vorticity equation (Equation (3)) assuming constant viscosity as

$$\frac{\partial \omega_z}{\partial t} + \frac{\partial}{\partial x_j}\left[u_j - \frac{\nu}{\omega_z}\frac{\partial \omega_z}{\partial x_j}\right]\omega_z = 0 \tag{4}$$

Equation (4) is similar to the equation used by Ogami and Akamatsu [20] in the development of the diffusion-velocity method.

By filtering Equation (4), the transport equation for the filtered spanwise component $\overline{\omega}_z$, developed for an eddy viscosity based SGS model, is obtained as [22]

$$\frac{\partial \bar{\omega}_z}{\partial t} + \frac{\partial[\bar{u} - ((\nu + \nu_{Tx})/\bar{\omega}_z)\partial\bar{\omega}_z/\partial x]\bar{\omega}_z}{\partial x} + \frac{\partial[\bar{v} - ((\nu + \nu_{Ty})/\bar{\omega}_z)\partial\bar{\omega}_z/\partial y]\bar{\omega}_z}{\partial y} = 0 \tag{5}$$

where $[\bar{u}_d = -((v+v_{Tx})/\bar{\omega}_z)\partial\bar{\omega}_z/\partial x,\ \bar{v}_d = -((v+v_{Ty})/\bar{\omega}_z)\partial\bar{\omega}_z/\partial y]$ are the components of the diffusion velocity governed by molecular diffusion and by the components of eddy viscosity from SGS model (v_{Tx}, v_{Ty}), and $\bar{u}$ and $\bar{v}$ are the components of the filtered velocity.

The Poisson's equation used in VIC method is obtained using the definition of the filtered spanwise component,

$$\bar{\omega}_z = \frac{\partial \bar{v}}{\partial x} - \frac{\partial \bar{u}}{\partial y} \tag{6}$$

Then using the filtered continuity equation,

$$\frac{\partial \bar{u}}{\partial x} + \frac{\partial \bar{v}}{\partial y} = 0 \tag{7}$$

the components of the velocity $\bar{\mathbf{u}}$ can be expressed as gradients of the stream function ψ,

$$\bar{u} = \frac{\partial \psi}{\partial y}, \quad \bar{v} = -\frac{\partial \psi}{\partial x} \tag{8}$$

Combining Equations (6) and (8), Poisson's equation is obtained as

$$\nabla^2 \psi = -\bar{\omega}_z \tag{9}$$

2.2. SGS models

The SGS models are function of the governing equations, i.e. vorticity transport or momentum transport. Few works using the vorticity transport are available. Mansfield *et al.* [14] obtained the constant in the Smagorinsky SGS model by balancing enstrophy production and dissipation for homogeneous and isotropic flow. Therefore, it has been adopted in this study. Furthermore, the Smagorinsky SGS model has been extended to anisotropic flow [37, 38] as

$$v_{Tx} = C_r^2(\Delta^3)^{2/9}\Delta_x^{4/3}(2S_{ij}S_{ij})^{1/2}$$

and

$$v_{Ty} = C_r^2(\Delta^3)^{2/9}\Delta_y^{4/3}(2S_{ij}S_{ij})^{1/2} \tag{10}$$

where $|S| \equiv (2S_{ij}S_{ij})^{1/2}$ is the modulus of the strain rate and the constant $C_r = 0.12$. Equation (10) is an extension of Smagorinsky model developed for isotropic flow to anisotropic flow by simply using different filter sizes Δ_x and Δ_y, in x and y directions, respectively, with $\Delta = (\Delta_x\Delta_y)^{1/2}$. The filter sizes are multiple (greater than one) of grid size. The Smagorinsky SGS model is too dissipative (see for example Reference [39]), therefore the less dissipative dynamic procedure developed in Reference [14] is also used.

The dynamic implementation requires calculating C_r at each node and at each time-step. As shown in Reference [14], two equations are generated. The first one is the 'filtered vorticity equation' using the physical filter size Δ and the second one is the filtered 'filtered vorticity equation' obtained using an additional test filter $\Delta' > \Delta$, in such a way that $\Delta' = 2\Delta$. Then the first equation is filtered again using the test filter and subtracted from the second equation assuming the same subgrid scale model in both equations. This yields an expression for the constant as

$$l = C_r^2 m \tag{11}$$

where

$$l = l^c + l^s \tag{12}$$

$$m = m^D + m^Z \tag{13}$$

For a 2D simulation

$$l^s = 0 \tag{14}$$

$$l^c = e_z \left\{ \overline{\overline{u}\,\frac{\partial \overline{\omega}_z}{\partial x}} + \overline{\overline{v}\,\frac{\partial \overline{\omega}_z}{\partial y}} - \overline{\overline{u}}\,\frac{\partial \overline{\overline{\omega}_z}}{\partial x} - \overline{\overline{v}}\,\frac{\partial \overline{\overline{\omega}_z}}{\partial y} \right\} \tag{15}$$

$$m^Z = 0 \tag{16}$$

$$m^D = e_z \Delta^2 \frac{\partial}{\partial x} \overline{\left\{ |\overline{S}| \frac{\partial \overline{\omega}_z}{\partial x} \right\}} + e_z \Delta^2 \frac{\partial}{\partial y} \overline{\left\{ |\overline{S}| \frac{\partial \overline{\omega}_z}{\partial y} \right\}}$$

$$- e_z \Delta'^2 \frac{\partial}{\partial x} \left\{ \overline{|\overline{S}|} \frac{\partial \overline{\overline{\omega}_z}}{\partial x} \right\} - e_z \Delta'^2 \frac{\partial}{\partial y} \left\{ \overline{|\overline{S}|} \frac{\partial \overline{\overline{\omega}_z}}{\partial y} \right\} \tag{17}$$

The constant C_r is uniquely specified in 2D simulation, unlike 3D simulation where the constant is over specified and error minimization is invoked. For any filtered variable calculated at the nodes, such as $\overline{\omega}_z$, double filtering, using either top-hat filter or Gaussian filter, is obtained using the differential interpretation of the filter where terms higher than second order are neglected [38].

2.3. *Vortex-in-cell*

The VIC methodology has been originated by Christiansen [40] and recent developments are discussed in Reference [5]. Also the methodology that extends the diffusion-velocity method to LES using an eddy viscosity SGS model and solves the vorticity transport using the vortex method is described in Reference [22]. In this section, a brief description of the method is presented. The vorticity field is discretized into N vortex blobs, each with circulation Γ_i. Therefore the vorticity field is expressed as $\omega(x) = \sum_{i=1}^{N} \Gamma_i \zeta_\sigma(\mathbf{x} - \mathbf{x}_i)$, where $\zeta_\sigma(\mathbf{x} - \mathbf{x}_i)$ is the smoothing function, $\mathbf{x}$ representing the coordinate at which the vorticity is calculated, $\mathbf{x}_i$ the coordinate of the centre of the vortex blob, and σ the core radius. The core radius is equal to the grid size and the circulation is identical to the product of vorticity and volume of the vortex blob. In VIC, the vorticity is transferred from the vortex blobs to the nodes of a grid, using an interpolation technique which is identical to the smoothing function. The area-weighting scheme [41] is used in this study. The components of the velocity $\mathbf{u} = (u, v)$ at the nodes are calculated using Equation (8) after solving the Poisson's equation (Equation (9)) using the extrapolated Liebmann's method. The components are transferred to the location of each vortex blob, using the area-weighting scheme. Then the vortex blobs are convected and the position vector of the vortex blob centre $\chi = (x_i, y_i)$ is calculated by integrating the

equation of motion of a material point

$$\mathrm{d}\chi/\mathrm{d}t = \mathbf{u}(\chi(x, y, z, t)) \tag{18}$$

using the improved Euler's method where the predictor is

$$\chi^*(t + \Delta t) = \chi(t) + \mathbf{u}\Delta t \tag{19a}$$

and the corrector is

$$\chi(t + \Delta t) = \chi(t) + (\mathbf{u} + \mathbf{u}^*)\Delta t/2 \tag{19b}$$

where Δt is the time-step and the values denoted by the superscript (*) correspond to the values obtained by the predictor.

After completing the above operation, the components of the diffusion velocities ($u_{di} = -((v + v_{Tx})/\bar{\omega}_z)\partial\bar{\omega}_z/\partial x$, $v_{di} = -((v + v_{Ty})/\bar{\omega}_z)\partial\bar{\omega}_z/\partial y$ are calculated at the nodes, and transferred to the centre of the vortex blob using the area-weighting scheme. Then the position vector of the vortex blob is calculated using Equations (19a) and (19b) in which $\mathbf{u} = \mathbf{u}_{di}$. The diffusion velocity could be unreasonably high in regions of a small vorticity and non-zero vorticity gradient because it is inversely proportional to the vorticity. This problem is remedied by setting the components of the diffusion velocity to zero whenever the vorticity at the nodes is less than 0.1% of the vorticity associated with a vortex particle.

The smoothing function is used in order to remove the singularity at the origin of the Biot–Savard Law, which relates the velocity to the vorticity. Otherwise large velocities are created in the neighbourhood of the discretized vortices, which causes numerical instabilities. To remove this difficulty, finite core size vortices or blob vortices are used instead of point vortices [42]. Thus inside the core, the velocity is smooth and is finite at the centre of the core. The smoothing function used in this study is the first-order area-weighting scheme. It distributes the vorticity of each vortex blob among the nearest four grid points (Figure 1(a)). That is the influence of each vortex blob extends to within one grid, with weight proportional to an area fraction, yielding a higher weight as the distance between the node and vortex blob is smaller. The more accurate third-order M_4' scheme has also been tested. It contributes to the nearest 16 grid points, i.e. its influence extends to within two grids. Flow field results for the present mixing layer obtained using the area-weighting scheme have been compared with the ones obtained using the M_4' scheme in Reference [22]. Results suggest that the sensitivity to the smoothing function is quite small probably because the number of vortex blobs used is high. Therefore the M_4' scheme was not used in the interest of reducing the computational time. The computational time is reduced by about 10% when the area-weighting scheme is used in comparison with the M_4' scheme.

It is noted that the finite-difference scheme equivalent to VIC may be based on (ψ, ω) formulation, i.e. on the solution of Equations (5) and (9). The VIC and finite-difference have in common the Poisson's equation (Equation (9)). Then in finite difference the vorticity transport is discretized and solved, whereas in VIC the equation of motion for a material point is used where the velocity used to convect the vortex blob is governed by the velocity obtained from the solution of Poisson's equation and by the diffusion-velocity. From a computational standpoint, the VIC requires additional memory because in addition to the vorticity and velocity calculated at the nodes which are common to both methods, the coordinates of the vortex blobs must be saved as time is marching.

2.4. Boundary and initial conditions

The computational domain in Figure 1(b) consists of a rectangular grid with uniform grid size in each direction and in general ($\delta_x \neq \delta_y$). The lower left corner of the grid is located at $x = 1$ and $y = 1$. The boundary conditions for LES are the same as for the unfiltered case because they are assumed to be governed by the large scale. The Neumann conditions apply to the inflow and outflow boundaries with $\psi_{0,0} = 0$ at $x = 0$ and $y = 0$. At inflow, two laminar boundary layers, which develop on high- and low-speed side of splitter plate, are

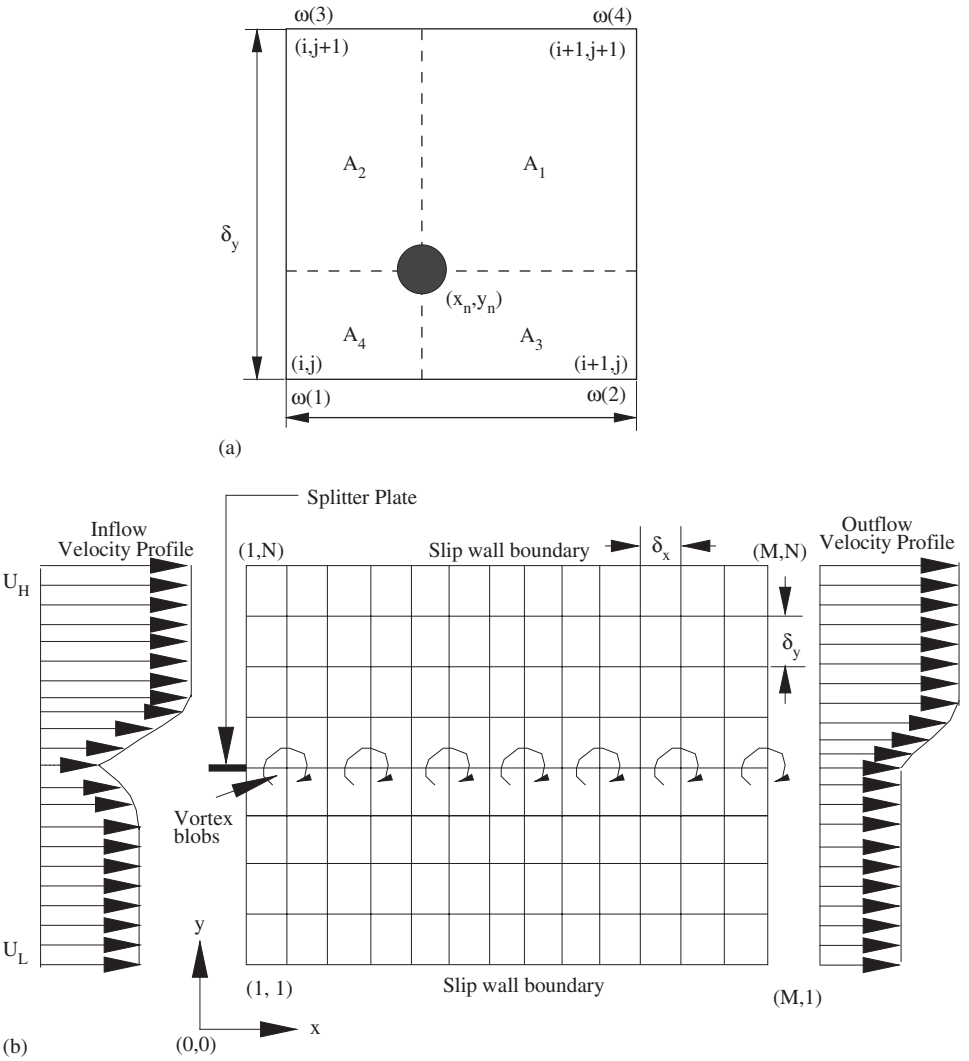

Figure 1. (a) Two-dimensional area-weighting scheme in the VIC method; and (b) computational domain, rectangular grid, initial position of the vortices and boundary conditions.

represented by fifth-order polynomials. Another fifth-order polynomial is used to patch the two boundary layers to avoid a zero velocity at the edge of the splitter plate. This will prevent the accumulation of Monte-Carlo particles at the node which is closest to the edge of the splitter plate. The Monte-Carlo particles are used in the solution method for the FDF equation (see Section 3.2). The inflow velocity profile reflects the development of the wake at some distance from the edge of the splitter. The outflow stream function profile corresponds to an error function velocity profile in such a way that,

$$(\partial\psi/\partial y)_{N,j} = (\Delta U/2)\,\mathrm{erf}\{\sigma(y - y_{ov})/(x - x_v)\} + U_c \tag{20}$$

where subscript N corresponds to the node in x direction at the outflow, j corresponds to the node in the y direction, $\Delta U = U_H - U_L$ is the velocity difference across the splitter plate, U_H and U_L are the velocities of the high- and the low-speed side, respectively, y_{ov} is the ordinate of the centreline, x_v is the virtual origin, σ is the spreading parameter and $U_c = (U_H + U_L)/2$ is the average velocity. In addition in order to simulate the Kelvin–Helmholtz instability mechanism, the vortex closest to the edge of the splitter plate is moved vertically by a small distance (perturbation), given by a sinusoidal function of time operating at the fundamental frequency (f), of the unforced mixing layer as

$$y(t) = Ax\sin(2\pi f t) \tag{21}$$

where $A = 0.5U_c\Delta t$ is the amplitude and x represents a small percentage of A ($x = 3.0\%$ in this study). The fundamental frequency (f) is calculated using $f\ \theta_i/(2U_c) \approx 0.02$ [43] where θ_i is the momentum thickness at the beginning of the region of linear growth. The factor A has been used by Inoue [11] where a forced mixing layer was investigated. In this study, the small value of $x = 3.0\%$ used ensures that the mixing layer is in the unforced mode.

Also rather than specifying an outflow boundary condition, i.e. Equation (21), the convective outflow boundary condition was considered. Results showed no significant difference up to $x/H \approx 0.25$, after which the momentum thickness growth rate is faster as compared to the situation where Equation (20) is applied. Therefore the error function outflow boundary condition has been adopted because it constrains the growth rate of the momentum thickness and yields a slope for the linear growth region in close agreement with the experiment [13].

Furthermore, slip conditions are assumed for the top and bottom boundaries. The Dirichlet condition is used for the bottom boundary located at $y_L = 1$ as,

$$\psi_{i,1} = y_L U_L \tag{22}$$

Equation (22) is consistent with $\psi_{i,0} = 0$ at $y = 0$. For the top boundary

$$\psi_{i,N} = U_L y_{\mathrm{sp}} + U_H(y_{i,N} - y_{\mathrm{sp}}) \tag{23}$$

where y_{sp} is the splitter plate y location and N corresponds to any node at the top boundary.

Initially, the velocity discontinuity across the splitter plate is simulated using a vortex sheet, which is discretized into a row of vortex blobs as shown in Figure 1(b). At time $t = 0$, the vortex blobs are equidistant and separated by a distance $d = L/M$, where M is the number of vortices and L is the computational domain length. The vortex closest to the edge of the splitter plate is moved vertically using Equation (21) to initialize the Kelvin–Helmholtz instability. The unfiltered total circulation in the computational domain is $L(U_H - U_L)$. The circulation is equally distributed among the M vortices as $\Gamma_i = L(U_H - U_L)/M = d(U_H - U_L)$. Furthermore,

if at the end of each time step Δt, defined as the characteristic time $\Delta t = d/U_c$, a vortex with circulation Γ_i is introduced at the trailing edge of the splitter plate, the vorticity generation rate is $\Gamma_i/\Delta t = (U_H - U_L)U_c$ and therefore the Kutta condition is satisfied. The oldest vortex, i.e. the vortex with the largest residence time, is discarded from the calculations when a new vortex is introduced at the edge of the splitter plate. Furthermore, the vortices can move freely in and out through the outflow boundary to avoid the collection of vortices at the end of the computational domain. The motion of the vortices outside the computational domain is assumed to be governed by the velocity at the outflow boundary. In the LES, the initial vorticity (or circulation) should be filtered. As discussed in References [14, 19], smoothing the vorticity field (or circulation) using $\zeta_\sigma(\mathbf{x} - \mathbf{x}_i)$, is an approximation of the filtered vorticity field, with the smoothing function acting as the spatial filter.

3. FDF'S TRANSPORT EQUATION

3.1. FDF transport

The transport equation for the FDF (P_L) of a non-reactive scalar, has been derived by filtering the fine-grained PDF to yield [29]

$$\frac{\partial(P_L)}{\partial t} + \frac{\partial(\overline{u}P_L)}{\partial x} + \frac{\partial(\overline{v}P_L)}{\partial y} = \frac{\partial}{\partial x}\left[(\Gamma + \Gamma_{Tx})\frac{\partial P_L}{\partial x}\right] + \frac{\partial}{\partial y}\left[(\Gamma + \Gamma_{Ty})\frac{\partial P_L}{\partial y}\right] - \frac{\partial^2}{\partial \xi^2}\left[\overline{\Gamma\left(\left|\frac{\partial \phi}{\partial x}\right|^2 + \left|\frac{\partial \phi}{\partial y}\right|^2\right)|\xi} P_L\right] \tag{24}$$

where $\Gamma = \nu/Sc$ is the molecular diffusivity, Sc is the Schmidt number, and Γ_{Tx} and Γ_{Ty} are the turbulent diffusivities related to ν_{Tx} and ν_{Ty} defined by Equation (10) via the turbulent Schmidt number Sc_T, as $\Gamma_{Tx} = \nu_{Tx}/Sc_T$ and $\Gamma_{Ty} = \nu_{Ty}/Sc_T$. The mixture fraction ϕ is defined as $\phi = (c - c_U)/(c_L - c_U)$, where c is the concentration of passive scalar, c_L and c_U are the concentrations below and above splitter plate.

In Equation (24), the three terms on the L.H.S. are in closed form. The first term is the transient term, the second and third terms are the convection terms. On the R.H.S., the first two terms represent the contributions of subgrid convective flux modelled using the gradient diffusion model via Γ_{Tx} and Γ_{Ty} and of molecular diffusion. The third term in which $[\overline{\Gamma(|\partial\phi/\partial x|^2 + |\partial\phi/\partial y|^2)|\xi}]$ indicates the expected value of $[\overline{\Gamma(|\partial\phi/\partial x|^2 + |\partial\phi/\partial y|^2)}]$ conditional on the satisfaction of the constraint ξ represents molecular mixing and is modelled using the modified Curl model. Pairs of particles that are within a grid are selected randomly as

$$n_m = \beta \overline{\omega}_f N_g \Delta t \tag{25}$$

where N_g denotes the total number of particles in the grid, n_m the number of pairs of particle that will mix, $\overline{\omega}_f$ is an average mixing frequency defined within the grid and the coefficient $\beta = 3$. Following Colucci *et al.* [29] and for the anisotropic flow considered in this study the mixing frequency is $\omega_f = C_\phi([(\Gamma + \Gamma_{Tx})/\Delta_x^2 + (\Gamma + \Gamma_{Ty})/\Delta_y^2]/2)$, where Δ_x and Δ_y are the

filter sizes in x and y directions, respectively, used in SGS models and $C_\phi \approx 3$. The mixing frequency at the location of a particle is obtained by transferring the mixing frequency from nodes to the particle using interpolation technique. Then the average mixing frequency $\overline{\omega}_f$ is approximated as the arithmetic average of the frequencies at the location of the particles which are within the grid.

3.2. Monte-Carlo simulation

The scalar FDF transport equation (Equation (24)) is solved using the Lagrangian Monte-Carlo method [44] rather than using the Eulerian method [25] because in the context of LES it is more accurate as pointed out by Colucci *et al.* [29]. The Monte-Carlo particles for scalar field governed by the FDF transport equation are different from the vortex particles for the flow field governed by vorticity transport. Therefore, the two systems of particles are used. Even though both systems are governed by similar physics, i.e. convection and diffusion, however initial conditions, magnitudes, and numerical approximations are different. This necessitates two different systems of particles. The Monte-Carlo particles are initially spread uniformly throughout the computational domain of Figure 2(b). Each particle is identified by a representative value of the scalar concentration ξ. Besides mixing discussed above, the particles are subjected to convection and turbulent transport. The time evolution of the particle position $X_i(t) = [x_i(t), y_i(t)]$ with property ξ is governed by the Langevin equation [44] given as

$$\mathrm{d}X_i(t) = D_i(X(t), t)\,\mathrm{d}t + E(X(t), t)\,\mathrm{d}W_i(t) \tag{26}$$

where D_i and E are the drift and diffusion coefficients, respectively, and W_i denotes the Wiener–Levy process. These coefficients are

$$D_i = (\overline{u}_i, \overline{v}_i) + \left(\frac{\partial(\Gamma + \Gamma_{Tx})}{\partial x_i}, \frac{\partial(\Gamma + \Gamma_{Ty})}{\partial y_i} \right)$$

and

$$E = (\sqrt{2(\Gamma + \Gamma_{Tx})}, \sqrt{2(\Gamma + \Gamma_{Ty})}) \tag{27}$$

The Wiener–Levy process is identical to the random walk obtained from a Gaussian distribution with zero mean and standard deviation $[2(\Gamma + \Gamma_{Tx})\Delta t]^{1/2}$ in x direction and $[2(\Gamma + \Gamma_{Ty})\Delta t]^{1/2}$ in y direction, respectively.

3.3. Boundary and initial conditions

The computational domain used for the Monte-Carlo simulation in Figure 2(b) is similar to the one used for flow field in Figure 1(b). The fast stream above the splitter plate has an initial concentration of $c_U = 0$, and the lower slow stream has an initial concentration of $c_L = 1$. Two inflow boundary conditions, stepwise profile and error function, will be tested. The error function is given as

$$c(y)_{1,j} = (\Delta c/2)\,\mathrm{erf}\{\sigma(y - y_{oc})/x_v\} + c_c$$

where subscript 1 corresponds to the inflow x-location and subscript j corresponds to the nodes in the y direction, $\Delta c = c_L - c_U$ is the concentration difference across the layer, $c_c = (c_L + c_U)/2$

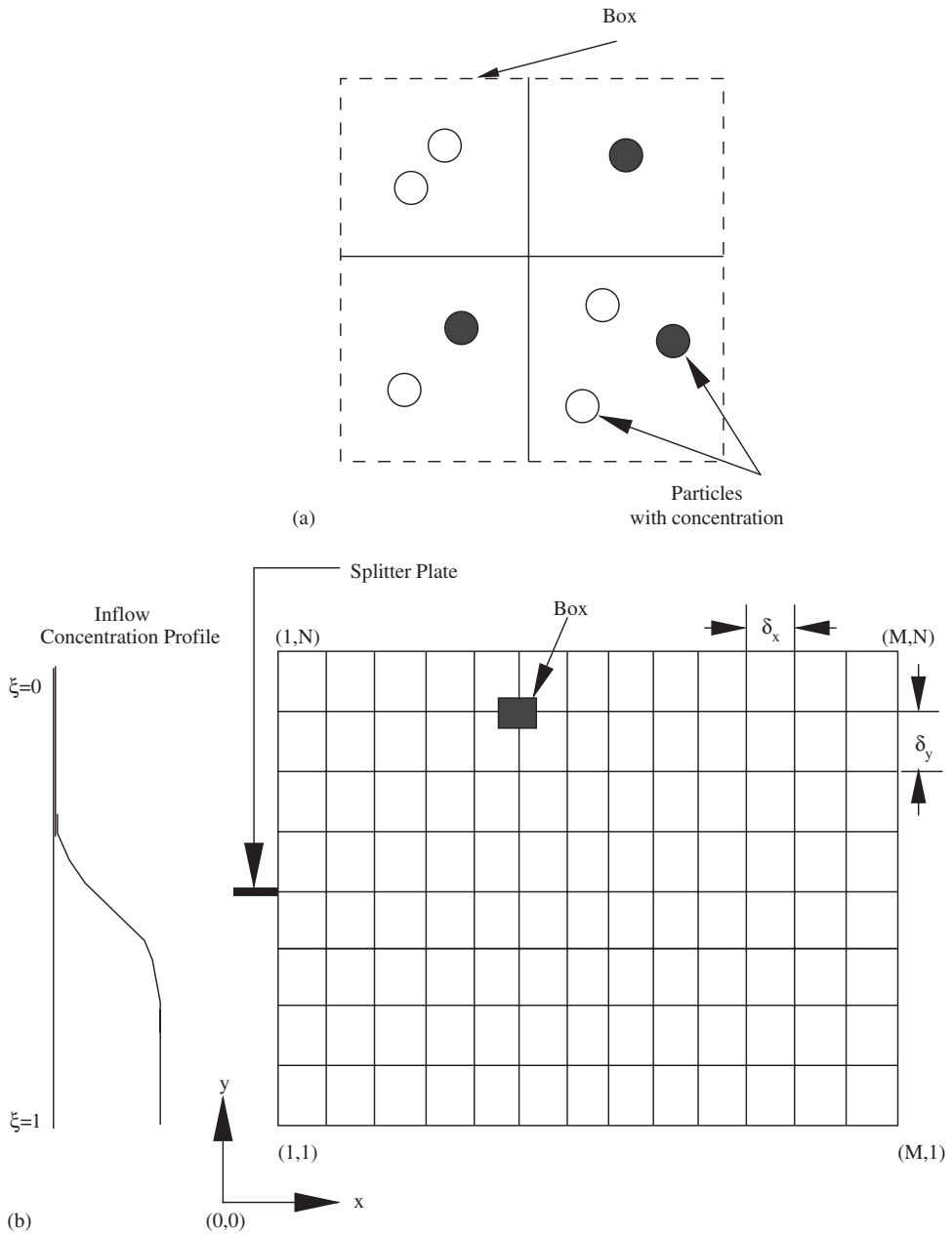

Figure 2. (a) Box centred at node and particles with concentration distribution; and (b) computational domain, rectangular grid, box and boundary condition for scalar field.

is the average concentration, σ is the spreading rate and y_{oc} is different from y_{ov}, the ordinate of centreline of velocity profile (Equation (20)). The relation $y_{oc} \neq y_{ov}$ is similar to the cross-stream adjustment length used in the 'wake-modified' inlet conditions by Soteriou and

Ghoneim [45], and is necessary in order to obtain predictions that fit the experimental data and previous numerical simulation. The outflow boundary condition is not specified (Equation (24) is parabolic) because the streamwise convection of concentration is very high in comparison with backward diffusion. Particles are allowed to exit the top, bottom, and the outflow boundaries of the computational domain. The domain is replenished at the boundary node which is opposite to the boundary node from which the particle exists. At inflow, the replenished concentrations are defined by the inflow boundary condition, stepwise or error function (Equation (28)), and at the top and bottom the concentrations assume the fast and slow free stream values of 0 and 1, respectively.

4. SOLUTION PROCEDURE

The solution procedure to solve the velocity, vorticity and scalar fields consists of the following steps:

(a) Initializing by placing the equidistant vortex blobs at the level of the splitter plate and by assuming arbitrary values for ψ at the internal nodes together with the boundary conditions (Equations (20)–(23)).
(b) Initializing the Monte-Carlo particles in the computational domain by prescribing particles to each grid.
(c) Assigning initial concentration to each particle, using either a stepwise profile with 0 above and 1 below the splitter plate, respectively, or the error function (Equation (28)).
(d) Transferring the vorticity from the vortex particles to the nodes using the interpolation technique.
(e) Solving the Poisson's equation (Equation (9)), using a Gauss–Seidel iteration with a left-to-right sweep of the nodes and bottom-to-top sweep of the lines. Iteration convergence is obtained when the percent difference between consecutive ψ is less than 0.001%.
(f) Computing the velocities $\bar{u}$ and $\bar{v}$ at the nodes using Equation (8).
(g) Transferring the velocities at the location of each vortex using the interpolation technique.
(h) Updating the coordinates of the vortices using the predictor equation (19a).
(i) Computing the SGS components of the eddy viscosity using Equation (10) with either $C_r = 0.12$ or dynamic calculations of C_r at each node (Equations (11)–(17)).
(j) Computing the components of diffusion velocity $(-((\nu+\nu_{Tx})/\bar{\omega}_z)\partial\bar{\omega}_z/\partial x, -((\nu+\nu_{Ty})/\bar{\omega}_z)\partial\bar{\omega}_z/\partial y)$ at the nodes.
(k) Transferring the diffusion-velocity at the location of each vortex using the interpolation technique.
(l) Updating the coordinates of the vortices using the predictor equation (19a).
(m) Calculating D_i and E using Equation (27) together with mixing frequency at the nodes.
(n) Implementing the corrector by repeating the calculations starting from (d), and replacing Equation (19a) by Equation (19b) in (h) and (l).
(o) Transferring D_i and E from the nodes to the location of the particles using interpolation technique.

(p) Displacing the particles by approximating Equation (26) using the corrector scheme (the concentration field does not affect the flow field therefore it is calculated after the flow field has been calculated).
(q) Updating the number of particles in grid together with the boundary conditions.
(r) Transferring the mixing frequency from the nodes to the location of the particles using interpolation technique, calculating the average mixing frequency in each grid, and obtaining the number of mixing pairs using Equation (25). The mixing pairs are selected and new concentrations are calculated.
(s) Introducing a new vortex at the edge of the splitter plate and discarding the oldest one.
(t) Marching in time by repeating the calculations from step (d)–(s).

The first and second derivatives are approximated using fourth-order central difference formulas.

5. FLOW FIELD RESULTS

The profiles of mean velocity, rms longitudinal (rmsu') and lateral (rmsv') velocity fluctuations, negative cross-stream correlation ($\overline{-u'v'}$), vorticity contours, and rms vorticity fluctuations (rmsω') are presented. The results of the LES with the dynamic eddy viscosity SGS model will be first presented. Then comparison with results obtained without SGS and with LES using Smagorinsky SGS will be discussed.

5.1. Flow field and numerical parameters

The velocity ratio is $r = U_L/U_H = 0.5$ (ratio of the lower velocity side of the splitter plate to the higher velocity side) with the free stream velocity above the splitter plate $U_H = 600\,\text{cm/s}$ and below the splitter plate $U_L = 300\,\text{cm/s}$, similar to the parameters used in the experiment of M and B [32]. The spreading rate is $\sigma = 35$ for $r = 0.5$ [46]. The reported results are for a viscous flow condition with $\nu = 14.5 \times 10^{-2}\,\text{cm}^2/\text{s}$ (the kinematic viscosity of air at 18°C).

The computational domain consists in a 256×256 anisotropic grid with equidistant grid, $\delta_x = 0.5\,\text{cm}$ and $\delta_y = 0.25\,\text{cm}$. The aspect ratio $a_{xy} = \delta_x/\delta_y = 2.0$ is consistent with $a_{xy} = 2.0$ used by Deardoff [47] and $a_{xy} = 3.7$ used by Shumann [48] in LES of channel flow. Kaltenbach [49] has reported that the representation of shear flows is most economical when an anisotropic grid (i.e. $a_{xy} > 1$) is used because it produces adequate values for ratios of rms velocity fluctuations as shown in Reference [22] where the ratios obtained from LES using Smagorinsky SGS were comparable to the ratios obtained without SGS when the grid is anisotropic. For all LES, the filter sizes are set to twice the grid size in each direction, i.e. $\Delta_x = 2\delta_x$ and $\Delta_y = 2\delta_y$. At the level of the splitter plate, the shear layer is discretized into a layer of $M = 2560$ equidistant vortex blobs. Therefore, the circulation of each vortex is $\Gamma_i = 1.5 \times 10^{-3}\,\text{m}^2/\text{s}$, and the time step $\Delta t = d/U_c = 11.1 \times 10^{-5}\,\text{s}$. The coordinate y_{ov} in Equation (20) is equal to 33 cm corresponding to the edge of the splitter plate.

The flow is allowed to develop for two residence times (i.e. $2M$ time-steps) before the statistical calculations are started. Then the mean flow is obtained using time-averaging over the next four residence times, and the rms velocity fluctuations, the negative cross-stream correlation and the rms vorticity fluctuations are calculated using time-averaging over the next eight residence times.

5.2. LES run with dynamic eddy viscosity SGS model

The streamwise mean velocity normalized as $(U-U_L)/(U_H-U_L)$ is shown in Figure 3(a) as a function of the similarity variable $\eta_v=(y-y_0)/(x-x_v)$ at four downstream locations, where U is the streamwise mean velocity, y_0 is the ordinate of the velocity centreline at x location, and the virtual origin defined as the x location at the intersection of the velocity centreline with the horizontal line at the level of the splitter plate is $x_v=4.01$ cm. The results of the numerical simulation are presented in the self-preserving region, which is from $x=51$ to 77cm,

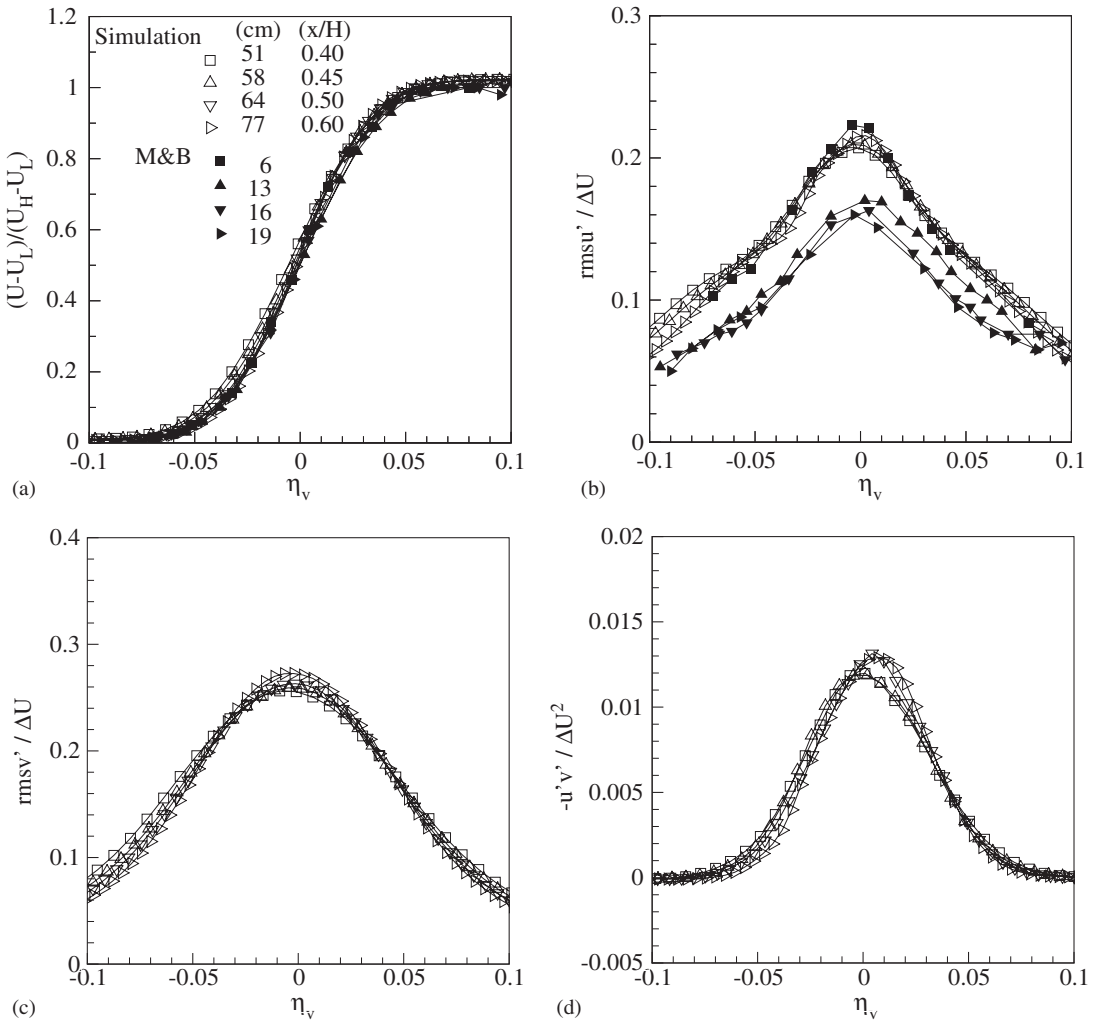

Figure 3. Normalized velocity profiles at four downstream locations for case with dynamic eddy viscosity SGS: (a) streamwise mean velocity; (b) rms longitudinal velocity fluctuations; (c) rms lateral velocity fluctuations; and (d) negative cross-stream correlation.

i.e. $0.4 \leqslant x/H \leqslant 0.6$. The self-preserving region corresponds to the region of linear growth of the momentum thickness. The profiles from the experiment of M and B [32] (dark symbols) are shown as a reference only because direct comparison between unfiltered experimental data and LES results (filtered) is unwarranted.

The rms longitudinal (rmsu') and lateral (rmsv') velocity fluctuations normalized with ΔU are shown in Figures 3(b)–(c), respectively, and the negative cross-stream correlation ($\overline{-u'v'}$) normalized with ΔU^2 is shown in Figure 3(d). Adequate self-preserving profiles are obtained for $0.4 \leqslant x/H \leqslant 0.6$. The rms$u'$ is shown together with the data from M and B [32]. The profiles for the rmsu' in the simulation are self-similar whereas it decreases in the experimental data. The experimental trend is probably caused by dissipation due to molecular diffusion as discussed in Reference [23].

5.3. *SGS effects*

Comparison between three runs is made: a run without SGS, LES using dynamic eddy viscosity SGS and LES using Smagorinsky SGS. Comparison with the run without SGS is made to verify whether the diffusion-velocity method predict the dissipative effect of SGS model. The LES run with dynamic eddy viscosity SGS is compared with Smagorinsky SGS to verify whether a lower eddy viscosity leads to less dissipation and therefore validate further the dissipative nature of the diffusion-velocity method when used in conjunction with a SGS model. Figures 4(a)–(c) show the downstream evolution of the spanwise vorticity contours for the three cases. Due to the inflow mean profile, the spanwise vorticity is initially negative (clockwise) in the computational domain. In the present two-dimensional case, this initial condition implies that the vorticity is always negative during the calculations. Therefore, Figures 4(a)–(c) show the magnitude of the vorticity. The contours spread in the free stream as they develop from the edge of the splitter plate. The maximum contour level decreases as SGS model is applied consistent with its dissipate nature (see legend). It is 1800 for the case without SGS in Figure 4(a), 1700 for the case with dynamic eddy viscosity SGS in Figure 4(b), 1400 for the case with Smagorinsky SGS model in Figure 4(c). Close up of selected downstream location are shown in Figures 5(a)–(c) which are drawn using identical scale. Figure 5(a) for the case without SGS indicates that the contours peak at 600, whereas the contour peak drops to 500 and 300 when dynamic eddy viscosity SGS and Smagorinsky SGS are used in Figures 5(b) and (c), respectively. The contour levels are further apart when SGS model is used. Therefore, in the context of the diffusion-velocity method, the SGS model is dissipative because it decreases the contour peaks and yields coarser contour lines. Furthermore, as expected, Smagorinsky SGS is more dissipative than dynamic eddy viscosity SGS [39]. This is consistent with the fact that in this study the dynamic constant C_r^2 was found to be less than the Smagorinsky constant $C_r^2 = 0.0144$. This results in lower eddy viscosity for dynamic SGS (see peak ν_{Tx}/ν in Table I).

Profiles of various statistics are shown in Figures 6(a)–(d) at $x/H = 0.6$ for the three cases discussed in the previous paragraph. The peaks of rms$u'/\Delta U$ and rms$v'/\Delta U$ in Figures 6(a) and (b), respectively, are higher for LES with dynamic eddy viscosity SGS as compared to the case with Smagorinsky SGS but lower than the case without SGS. This is again consistent with the fact that the dynamic eddy viscosity model is less dissipative than Smagorinsky model. The negative cross-stream correlation ($\overline{-u'v'}/\Delta U^2$) in Figure 6(c) is less affected by SGS, consistent with being linked to the mean by the mean momentum equation and the mean

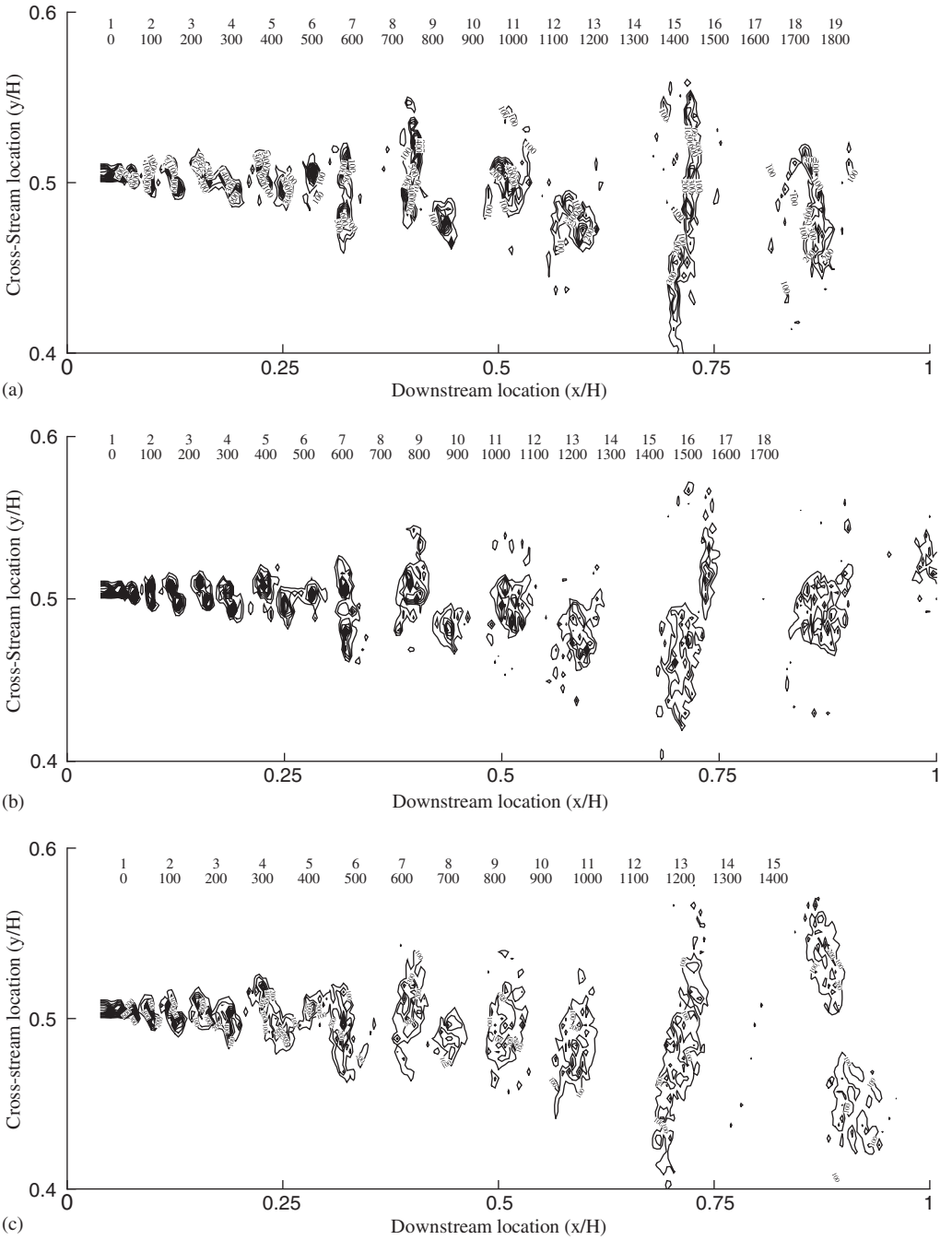

Figure 4. Vorticity contours for case: (a) without SGS; (b) with dynamic eddy viscosity SGS; and (c) with Smagorinsky SGS. Contour-level increment is 100.

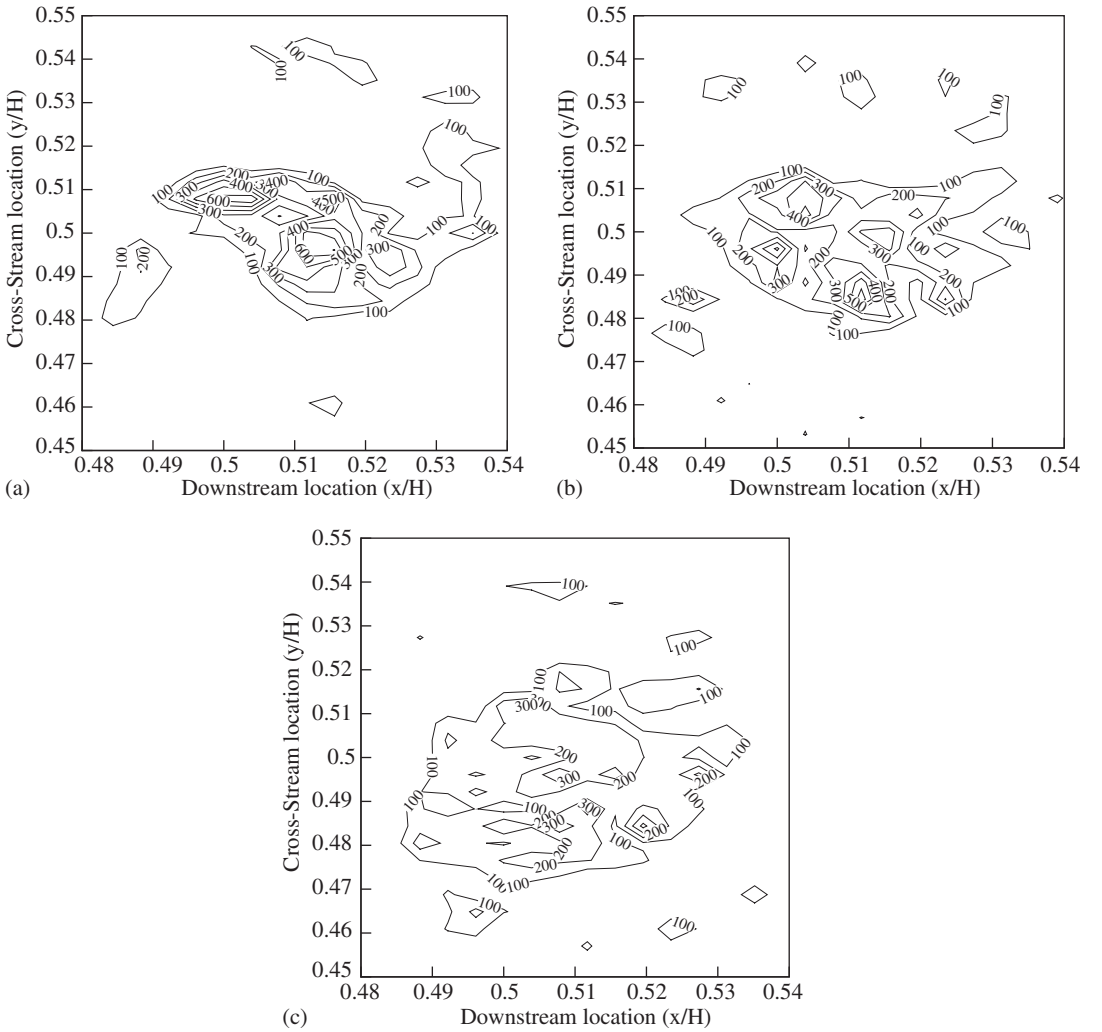

Figure 5. Vorticity contours at selected downstream location for case: (a) without SGS; (b) with dynamic eddy viscosity SGS; and (c) with Smagorinsky SGS. Contour-level increment is 100.

Table I. Effect of SGS on v_{Tx}/v and rmsu'/rmsv' at $x/H = 0.6$.

C_r	Peak v_{Tx}/v at last time-step	rmsu'/rmsv' at peak
0 (without SGS), △	0	0.812
Dynamic calculations, ◁	10	0.808
0.12 (Smagorinsky SGS)	24	0.788

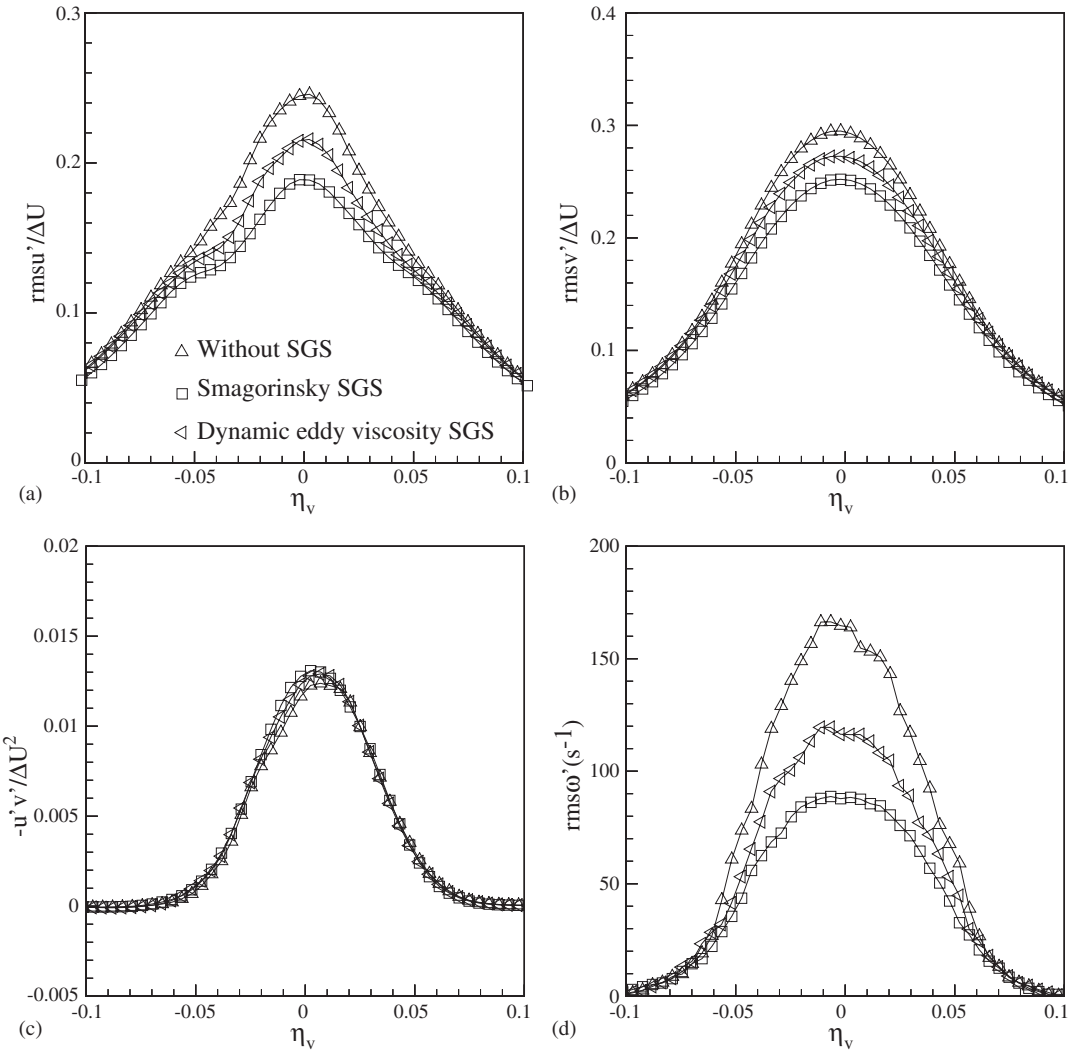

Figure 6. Comparison of profiles with and without SGS model: (a) rms longitudinal velocity fluctuations; (b) rms lateral velocity fluctuations; (c) negative cross-stream correlation; and (d) rms vorticity fluctuations at $x/H = 0.6$.

flow is slightly affected by SGS as found in Reference [22]. The peak rmsω' in Figure 6(d) is lowered as the dissipative effect of SGS is increased, consistent with the lower contour level peaks in Figures 4(a)–(c) and 5(a)–(c). Table I also shows that the ratio rmsu'/rmsv' for LES using dynamic eddy viscosity model is closer to the case without SGS than the LES with Smagorinsky model. Furthermore, Figures 7(a)–(b), show rms$u'/\Delta U$ and rms$v'/\Delta U$ profiles for LES using Smagorinsky SGS. By comparing with the profiles obtained using dynamic eddy viscosity SGS in Figures 3(b)–(c), it is noted that the profiles obtained using the dynamic procedure have a better self-similarity.

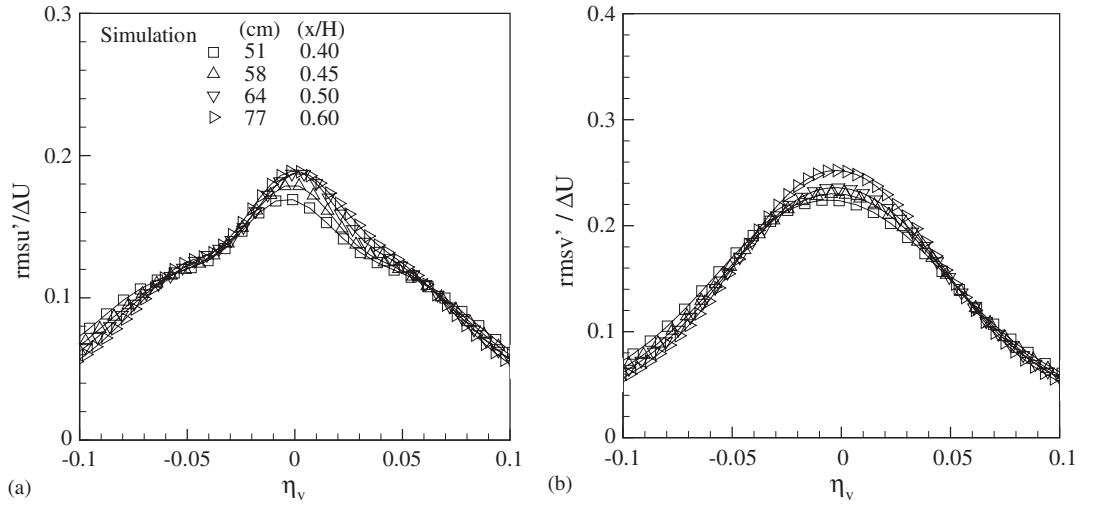

Figure 7. Velocity profiles at four downstream locations for case with Smagorinsky SGS: (a) rms longitudinal velocity fluctuations; and (b) rms lateral velocity fluctuations.

6. SCALAR FIELD RESULTS

The scalar field calculations are conducted on rectangular computational domain identical to the flow field computational domain. The initial number of particles per grid is $N_g = 36$ which is within the range 20–200 suggested in Reference [30]. The mean concentration, rms concentration fluctuations and FDFs are approximated at the nodes using particles located in rectangular boxes centred at nodes (Figure 2(a)). The boxes do not overlap, i.e. the box size is less than half the grid size. The approximation becomes more accurate as the box size is decreased and as the number of particles is increased. In this study, the box size is 0.4 of grid size. For each particle, at time $t = 0$ the concentration is initialized as $c_L = 1.0$ on the low-speed stream and $c_U = 0.0$ on the high-speed stream. Both Smagorinsky SGS and dynamic eddy viscosity SGS are tested. Two inflow boundary conditions for scalar field are also tested, stepwise and error function with $y_{oc} = 31.8$ cm in Equation (28). The run using dynamic eddy viscosity SGS model with error function as boundary condition for scalar is chosen as the base run.

The FDF solution requires specifying the constants Sc_T, C_ϕ, and the mixing model. For the base run, the modified Curl model is used with $C_\phi = 3.0$ and $Sc_T = 0.7$ similar to the ones used in Reference [31]. Effects of Smagorinsky SGS, Sc_T, C_ϕ and inflow boundary conditions on mean concentration, rms concentration fluctuations and FDF will be discussed.

To achieve statistically stationary solutions, the Monte Carlo simulation is run for 14 residence times similar to the flow field run. Firstly, the flow is allowed to develop in the first two residence times, then the mean concentration is computed over the next four residence times. The rms concentration fluctuations and FDF are computed over the next eight residence times.

6.1. Mean concentration, RMS concentration fluctuations and concentration spread for base run

Figures 8(a)–(b) show the mean concentration ($\overline{\xi}$) plotted as a function of the similarity variable $\eta_c = (y - y_c)/(x - x_{vc})$, where y_c is the concentration centreline at streamwise location x, and x_{vc} is the x location of the virtual origin for concentration. Figures 8(a) and (b) show that the results of the simulation are close to the experiment of M and B [32] and to the simulation of Zhou and Pereira [31], respectively, for $0.5 \leqslant x/H \leqslant 0.6$. For $x/H = 0.4$, the mean concentration profile is in the non self-preserving region unlike the mean velocity

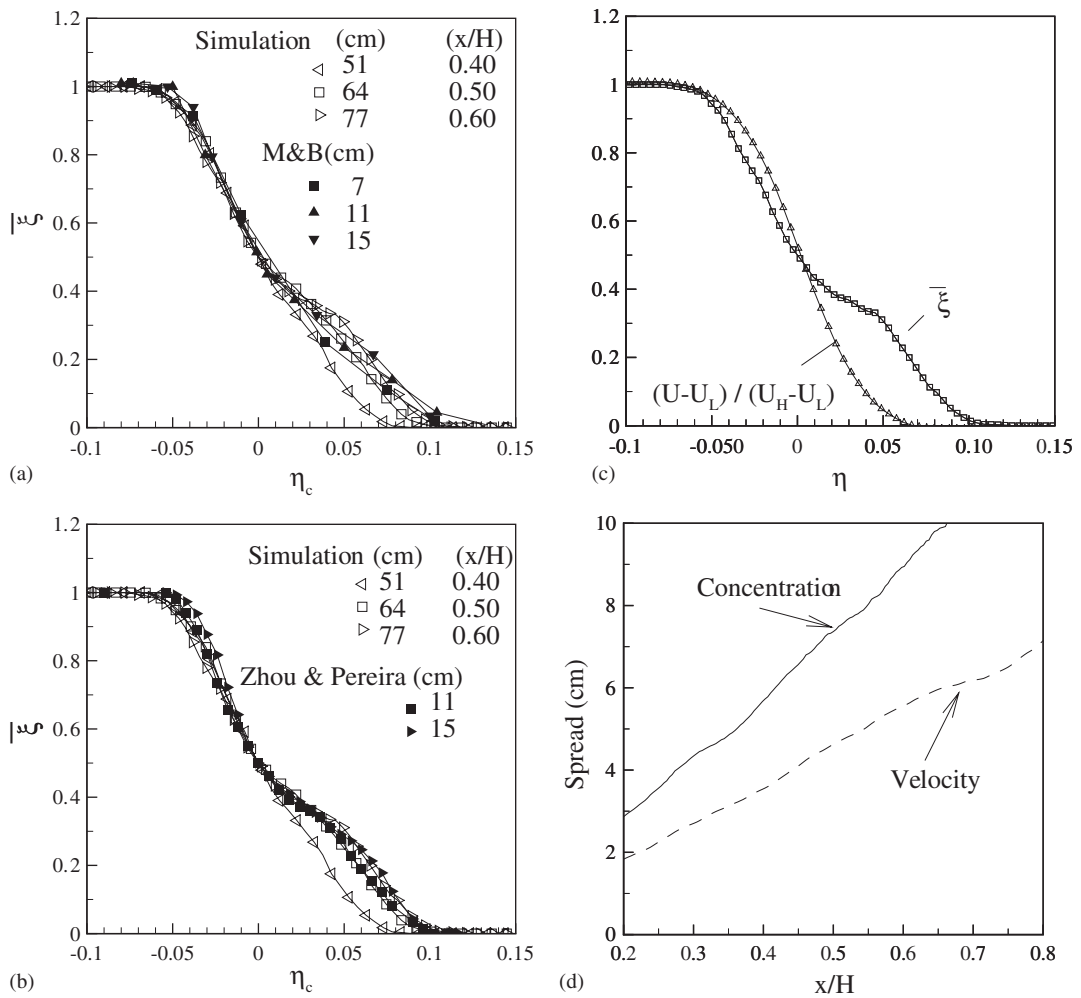

Figure 8. (a, b) Mean concentration at three downstream locations for base run; (c) mean concentration profile and normalized mean velocity profile at $x/H = 0.6$ for base run; and (d) spread of concentration and velocity for base run.

profile which is in the self-preserving region (see Figure 3(a)). Furthermore, the free stream concentration extends further on the high-speed side ($\eta_c > 0$) than on the low-speed side ($\eta_c < 0$). This shows that the mixing layer entrains more particles from the high-speed fluid. The mean concentration profiles exhibit triple inflection point for $x/H = 0.5$ and 0.6 similar to References [31, 32]. However for $x/H = 0.4$, the triple inflection point is less pronounced, because the flow is still developing. Figure 8(c) shows the mean concentration profile and the mean velocity profile at $x/H = 0.6$. The concentration mixing region extends further into the free stream than does the momentum mixing region as found in Reference [32]. This result is consistent with Figure 8(d), which indicates that the concentration spread is higher than the velocity spread. The velocity spread is characterized by the region between $0.05U_L$ and $0.95U_H$ and the concentration spread by the region with concentration between $\xi = 0.05$ and 0.95.

The rms concentration fluctuations profiles (ξ_{rms}) are shown as a function of η_c at three downstream positions in Figures 9(a) and (b). The rms concentration fluctuations is indicative of the degree of homogeneity of the flow. If the two streams were composed of immiscible substances, then the rms concentration fluctuations would have a maximum value of 0.5. The calculated rms concentration fluctuations is lower than 0.5 but slightly higher than the measurements of M and B [32] in Figure 9(a) and close to the results of Zhou and Pereira [31] in Figure 9(b). The rms concentration fluctuation profiles exhibit bimodal shape and asymmetry with respect to $\eta_c = 0$ with values on the high-speed side ($\eta_c > 0$) lower than the low-speed side ($\eta_c < 0$). This indicates that fluid mixing is higher on the high-speed side. In the simulation, the bimodal shape in the ξ_{rms} profiles together with the asymmetry with lower ξ_{rms} on the high-speed side were obtained, when error function was used as inflow boundary condition for scalar field (see Section 6.5).

In order to interpret the asymmetry with respect to $\eta_c = 0$ in the rms profiles, the instantaneous mixing frequency in the cross-stream location is shown in Figures 10(a)–(d) at several

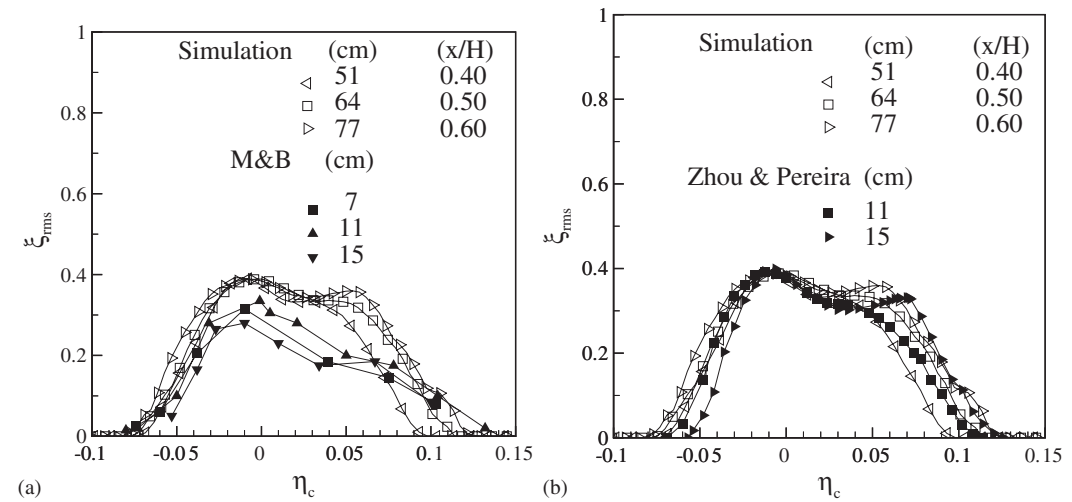

Figure 9. (a, b) rms concentration fluctuations profiles at three downstream locations for base run.

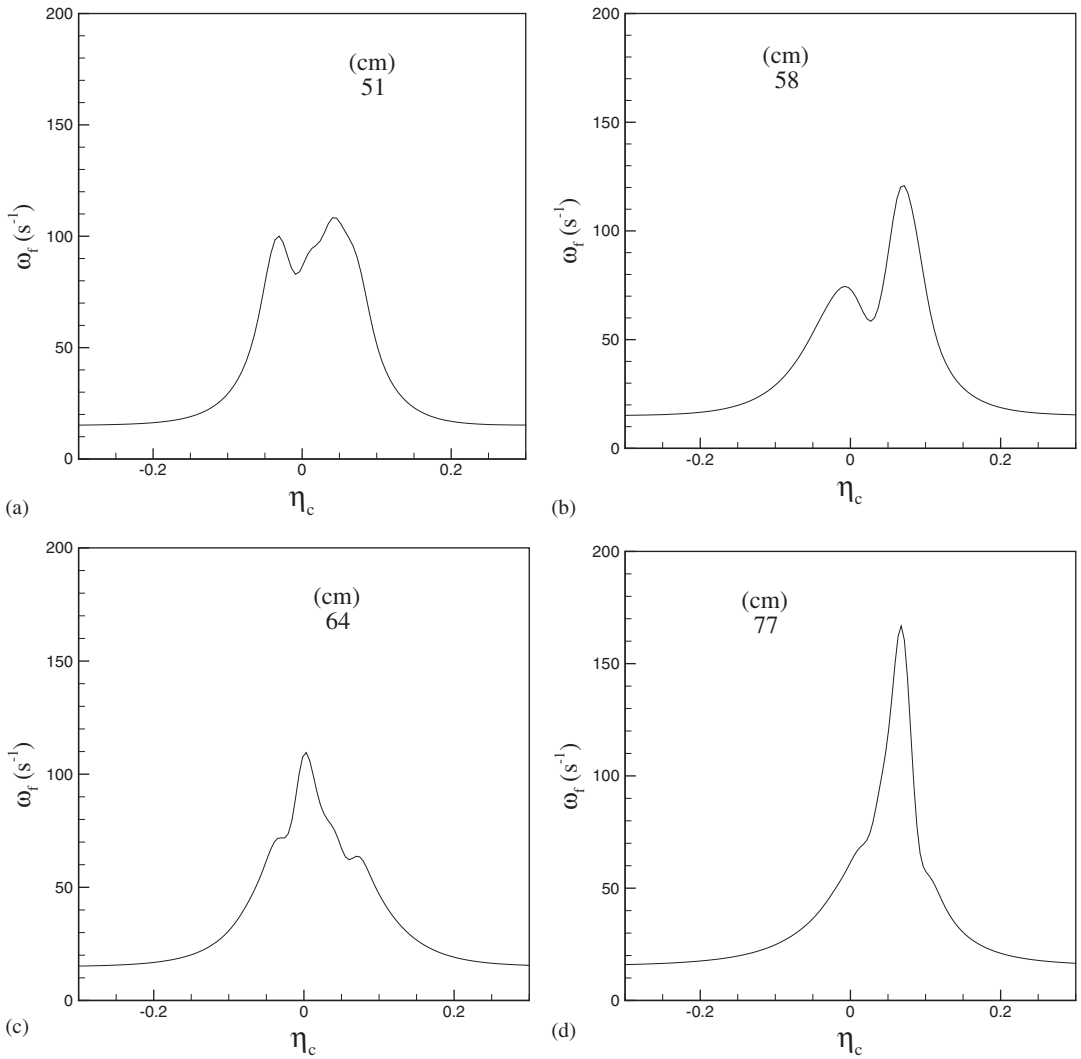

Figure 10. Profiles of mixing frequency versus η_c at several downstream locations: (a) $x/H = 0.40$; (b) $x/H = 0.45$; (c) $x/H = 0.50$; and (d) $x/H = 0.60$.

streamwiselocations from $x/H = 0.4–0.6$. The mixing frequency is asymmetric about the concentration centreline with higher values biased toward the high-speed side therefore leading to lower ξ_{rms} on the high-speed side in Figures 9(a) and (b). Therefore, the asymmetry in mixing frequency is responsible for the asymmetry in ξ_{rms} as shown also by Vanormelingen and Den Bulck [50].

6.2. Mean and RMS concentration fluctuations profiles for Smagorinsky SGS model

Figures 11(a)–(d) show that the profiles of mean concentration and rms concentration fluctuations, using the Smagorinsky SGS with $C_r = 0.12$ together with the experiment of M and

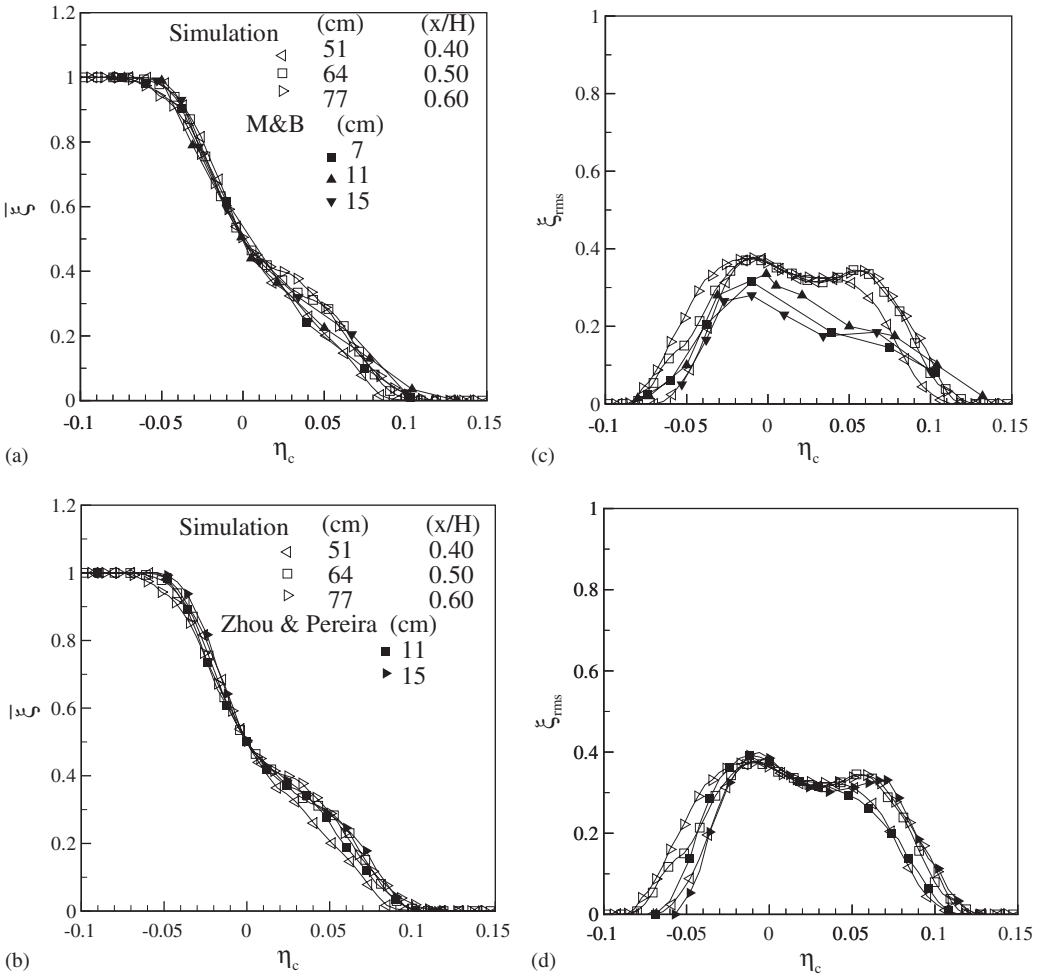

Figure 11. Mean concentration and rms concentration fluctuations profiles at three downstream locations using Smagorinsky SGS: (a, b) mean concentration profiles; and (c, d) rms concentration fluctuation profiles.

B [32] and simulation of Zhou and Pereira [31]. The profiles are similar to the results obtained using dynamic eddy viscosity SGS. For $x/H = 0.4$, the mean concentration profile in Figures 11(a) and (b) is closer to the self-similarity region, unlike the results obtained using the dynamic eddy viscosity SGS in Figures 8(a) and (b). This is probably due to the fact that the concentration field develops faster when Smagorinsky SGS is used because it is more dissipative. Calculations with Smagorinsky SGS yield higher turbulent diffusivities and higher mixing frequency than the ones obtained using dynamic SGS.

6.3. Effect of turbulent Schmidt number

Numerical tests were performed to investigate the effects of varying turbulent diffusivities using $Sc_T = 0.3$ and 1.0 with other parameters similar to base run. The range of Sc_T includes

the value of 0.5 used for plane mixing layer [51] and the value of 0.35 for the scalar mixing layer experiment of Bilger *et al.* [52]. In Figure 12(a), the mean concentration profiles show that the position of inflection points on the high-speed side moves further on high-speed side for $Sc_T = 0.7$ as compared to the profile with $Sc_T = 1.0$, and that the triple inflection point profile is less pronounced for $Sc_T = 0.3$. The profile with $Sc_T = 0.7$ is closer to the experiment

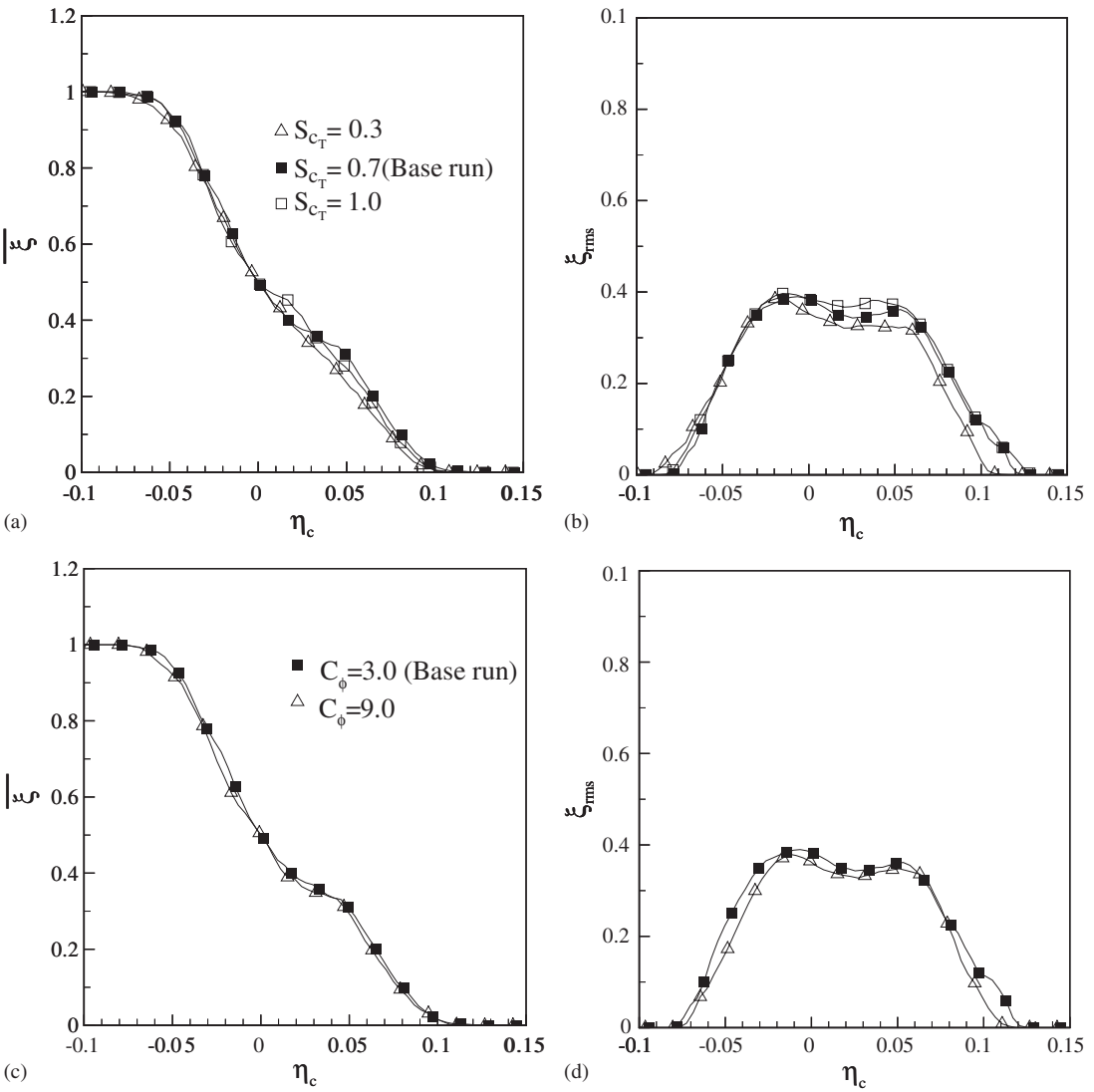

Figure 12. Comparison of mean concentration profiles: (a) effect of Schmidt number (Sc_T); (c) effect of constant (C_ϕ) in mixing frequency, at $x/H = 0.60$. Comparison of rms concentration fluctuation profiles: (b) effect of Schmidt number (Sc_T); and (d) effect of constant (C_ϕ) in mixing frequency, at $x/H = 0.60$.

of M and B [32] and to the simulation of Zhou and Pereira [31] as shown in Figures 8(a) and (b). Figure 12(b) shows that the profiles of rms concentration fluctuations are lowered as Sc_T is decreased from 1.0 to 0.3, because mixing frequency increases as Sc_T decreases. Also the profiles spread further into the free stream on high speed for $Sc_T = 0.7$ and 1.0 as compared to $Sc_T = 0.3$.

6.4. *Effect of constant in mixing frequency*

The effect of constant in mixing frequency was investigated by comparing the base run results ($C_\phi = 3.0$) with the results obtained using $C_\phi = 9.0$ keeping all other parameters similar to base run. The mean concentration profiles in Figure 12(c) exhibit triple inflection point for both $C_\phi = 9.0$ and 3.0. In Figure 12(d), the profile of the rms concentration fluctuations with $C_\phi = 9.0$ is lower than the base run with $C_\phi = 3.0$. This result is expected because the mixing is enhanced as C_ϕ is increased. This causes the profile of rms concentration fluctuations to be lowered.

6.5. *Effect of inflow boundary condition*

Several combinations of inflow boundary conditions were tested. Error function and laminar boundary layer were tested for flow field, and stepwise and error function for scalar field. Results are presented in Figures 13(a)–(d) and 14(a)–(f). Figures 13(a)–(d) compare the flow field characteristics, i.e. $(U-U_L)/(U_H-U_L)$, rms$u'/\Delta U$, rms$v'/\Delta U$ and $(\overline{-u'v'}/\Delta U^2)$ profiles, obtained using the laminar boundary layer with the ones obtained using the error function, at $x/H = 0.5$ and 0.6. The difference in profiles due to the different inflow boundary conditions for flow field is quite small. Therefore the velocity characteristics are not significantly affected by the inflow boundary conditions tested.

Figures 14(a)–(d) compare the runs using stepwise profile as inflow boundary condition for scalarfield with laminar boundary layer (case 1) and error function (case 2) for flow field. Figures 14(a) and (c) show that the mean profiles for cases 1 and 2 spread less than the base run. Figures 14(b) and (d) show that the rms concentration fluctuations profiles for cases 1 and 2 have higher peak values on the high-speed side ($\eta_c > 0$) as compared to the low-speed side ($\eta_c < 0$), which is opposite to the results obtained using the base run.

Figures 14(e) and (f) compare the runs using error function as inflow boundary condition for scalar field with laminar boundary layer (base run) and error function (case 3) for flow field. The mean concentration profiles in Figure 14(e) show that a portion of the graph for case 3 on the high-speed side is lower than the base run. Figure 14(f) indicates that the trend in the rms concentration fluctuations profiles is almost unaffected by inflow boundary condition for flow field (base run or case 3), except that the profile for case 3 spreads further on both the high-speed side ($\eta_c > 0$) and low-speed side ($\eta_c < 0$).

6.6. *Filtered density function*

Each particle of the ensemble N_b (total number of particles in the box centred at each node) is identified by a value of the concentration c with $0 \leqslant c \leqslant 1$. In order to obtain the probability, the range of c (0–1) is subdivided into 100 windows, so that any one of the particles belongs to an interval based on its value of c. The probability of finding a particle having concentration c within an interval

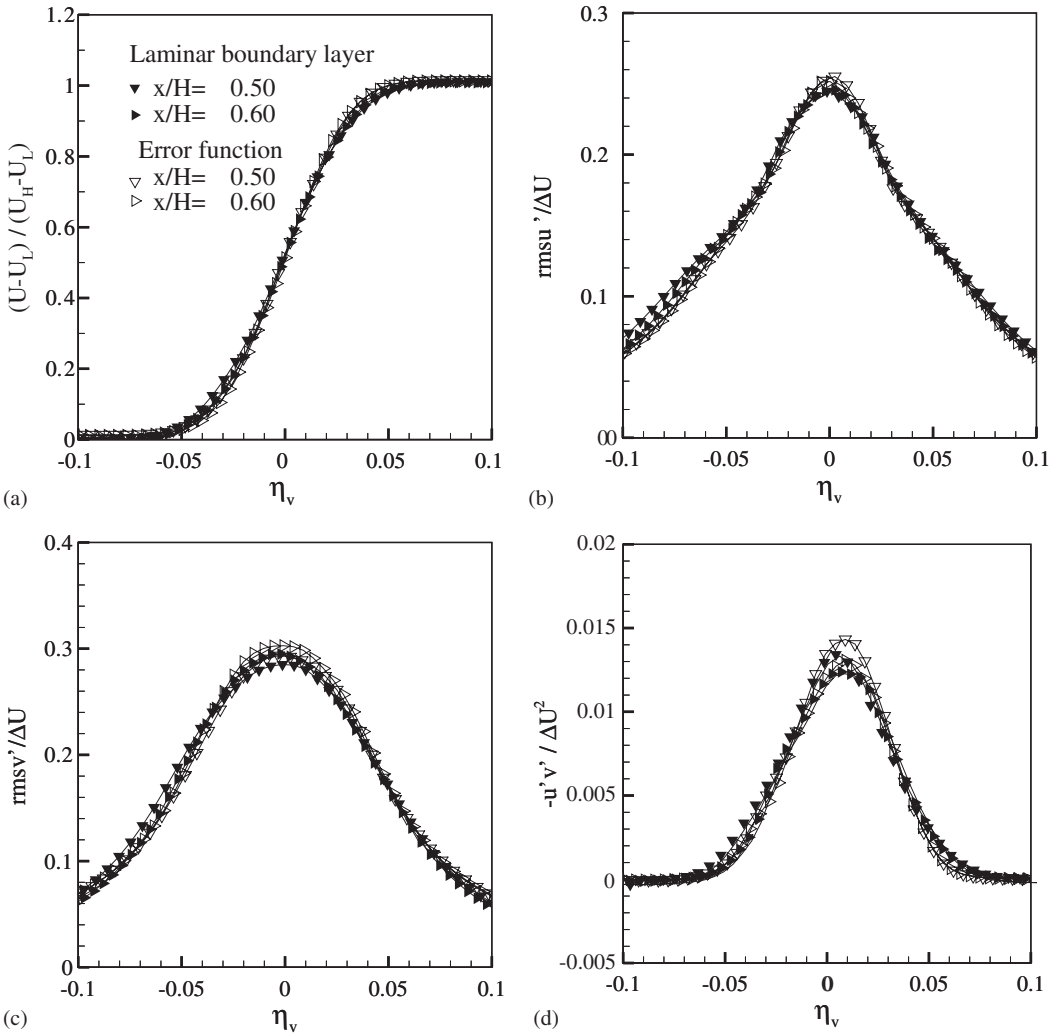

Figure 13. Effect of inflow boundary conditions on flow field, laminar boundary layer versus error function at two downstream locations: (a) streamwise mean velocity; (b) rms longitudinal velocity fluctuations; (c) rms lateral velocity fluctuations; and (d) negative cross-stream correlation.

$\zeta \preceq c \prec \zeta + \Delta\zeta$ is written as

$$p(\zeta)\Delta\zeta = \frac{n}{N_b}$$

where n is the number of elements in the interval and $p(\zeta)$ is the FDF.

The FDF of passive scalar obtained using dynamic eddy viscosity SGS (base run) are shown in Figures 15(a), (c), and (e) and the corresponding mean concentration profiles in

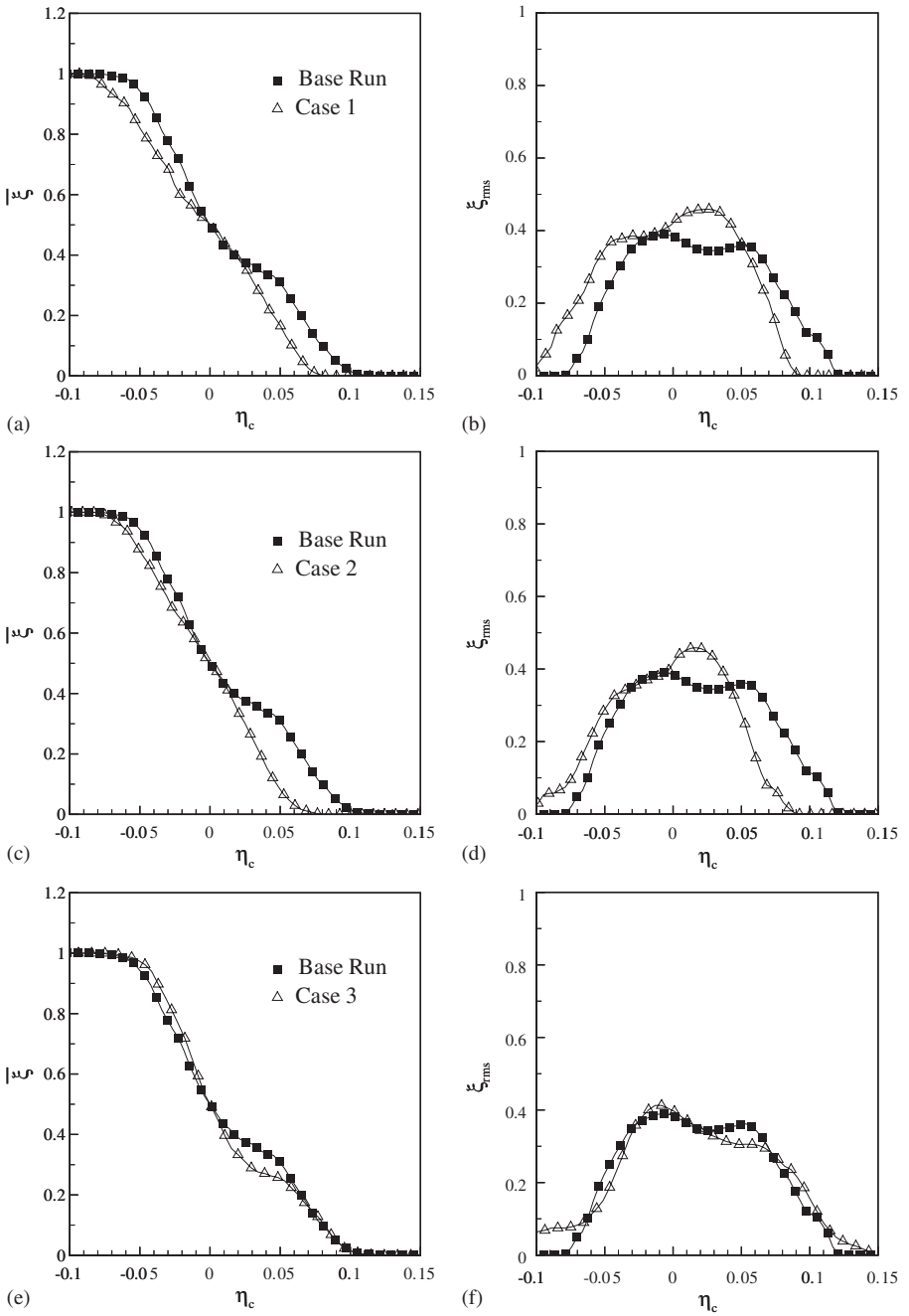

Figure 14. Effect of inflow boundary conditions (a, c, e) mean concentration profiles; and (b, d, f) rms concentration fluctuations profiles, at $x/H = 0.60$. Base run: laminar boundary layer flow filed and error function scalar field. Case 1: Laminar boundary layer flow field and stepwise scalar field. Case 2: Error function flow field and stepwise scalar field. Case 3: Error function flow field anderror function scalar field.

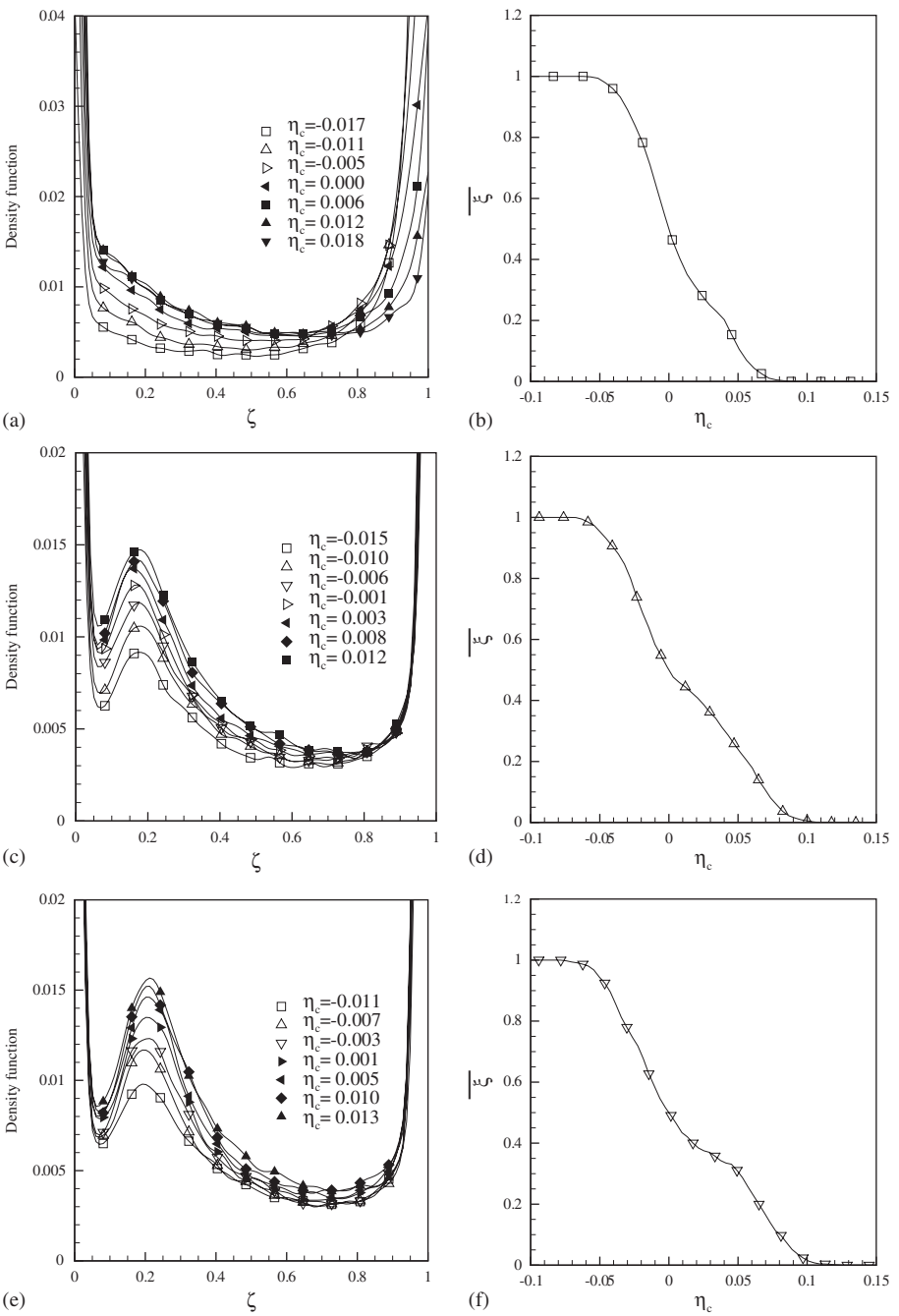

Figure 15. Filter density functions at several cross-stream locations for base run: (a) $x/H = 0.4$; (c) $x/H = 0.5$; (e) $x/H = 0.60$. Mean concentration profile for base run: (b) $x/H = 0.4$; (d) $x/H = 0.5$; and (f) $x/H = 0.6$.

Figures 15(b), (d), and (f) for $x/H = 0.4, 0.5$ and 0.6, respectively. At $x/H = 0.40$, the FDF in Figure 15(a) have U shape in qualitative agreement with the experiment of Pickett and Ghandhi [35] in the early part of the flow development. The mean concentration profile in Figure 15(b) indicates that the triple inflection point profile is starting to appear. As the flow develops from $x/H = 0.5$ (Figure 15(c)) to $x/H = 0.6$ (Figure 15(e)), the FDF exhibit intermediate peaks on high-speed side ($\zeta < 0.5$) that are non-marching. This indicates that the mixing layer entrains and subsequently mixes more particles from the high-speed side. These results are in agreement with the results of Koochesfahani and Dimotakis [53] and Pickett and Ghandhi [35]. Furthermore the mean concentration profiles in Figures 15(d) and (f) indicate that the triple inflection profile becomes more pronounced as the flow develops from $x/H = 0.5$ to 0.6.

Figures 16(a)–(d) compare FDF of four cases: effect of downstream location, effect of SGS, effect of C_ϕ and effect of Sc_T. Effect of downstream location shown for base run in Figure 16(a), at two y locations above ($\eta_c > 0$) and below ($\eta_c < 0$) centreline, show that the peak moves from $\zeta \approx 0.18$ for $x/H = 0.5$ to $\zeta \approx 0.23$ for $x/H = 0.6$. Also the peak values are higher at $x/H = 0.6$, i.e. at the downstream location which is further away from the edge of the splitter plate. These results are in qualitative agreement with M and B [32]. Figure 16(b) compares FDF obtained using Smagorinsky SGS with the ones obtained using dynamic eddy viscosity SGS (base run). The peak obtained using Smagorinsky SGS is higher than the peak obtained using the dynamic eddy viscosity SGS. Also the position of the peak is closer to the mean value ($\zeta = 0.5$) when Smagorinsky SGS is used. This is probably due to the fact that Smagorinsky SGS is more dissipative. In the calculations, Smagorinsky SGS yields higher mixing frequency than that of dynamic SGS. Higher mixing results in higher probabilities at peaks and also peak positions closer to the mean value ($\zeta = 0.5$). Figure 16(c) compares FDF obtained using $C_\phi = 9.0$ in mixing frequency with base run ($C_\phi = 3.0$). The peak is higher when $C_\phi = 9.0$ and slightly closer to the mean value ($\zeta = 0.5$). This result is expected because mixing (mixing frequency) is enhanced as C_ϕ is increased. The effect of varying Sc_T is shown in Figure 16(d). As Sc_T is decreased, the peak values are higher and closer to the mean value ($\zeta = 0.5$). This result is due to the fact that mixing (mixing frequency) is enhanced as Sc_T decreases.

The FDF trends are sensitive to scalar field inflow boundary conditions. In addition to the error function used in base run, a stepwise profile was tested. The FDF obtained using the stepwise profile yielded U shape FDF without peak, unlike the FDF for base run in Figures 16(a), (c), and (e).

7. COMPUTATIONAL REQUIREMENTS AND SENSITIVITY TO PARAMETERS

Table II shows the computational time and memory requirements for several simulations obtained using a PC with AMD Athlon 64 processor. The VIC's computational time is significantly less than that of the VIC-FDF, it is about 2% of the VIC-FDF. Computational time for finite difference-FDF simulation with same numerical and flow parameters is not available in order to compare with the present VIC-FDF. It is expected that CPU time of finite difference-FDF be less than that of VIC-FDF because the Lagrangian procedure in VIC requires higher CPU time. In the present study, CPU time of VIC is much less than VIC-FDF, therefore the advantage of finite difference-FDF over VIC-FDF, as it requires less CPU time, is minor.

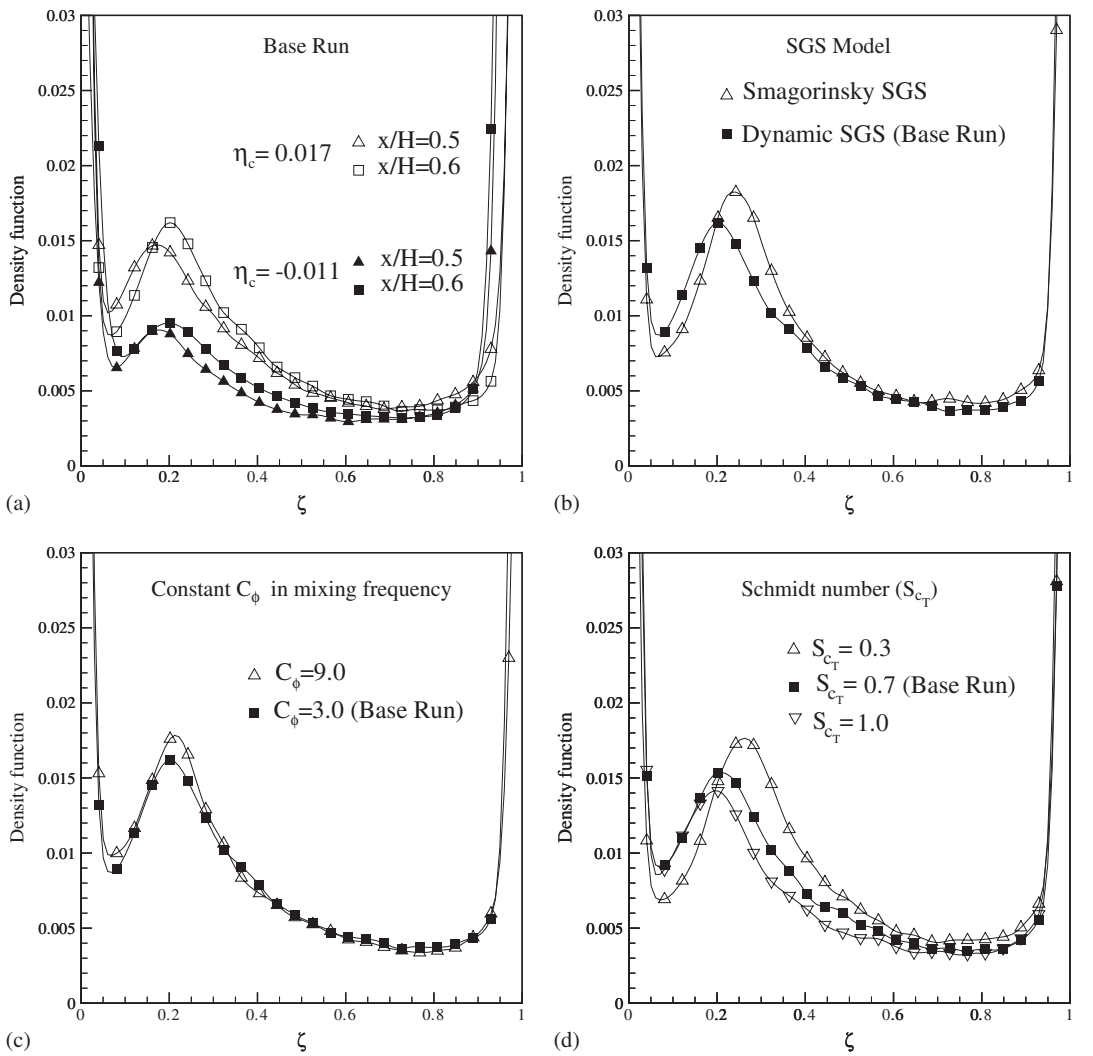

Figure 16. Comparison of filtered density functions: (a) effect of downstream location, $x/H = 0.5$ and $x/H = 0.6$; (b) effect on SGS at $x/H = 0.6$; (c) effect of C_ϕ at $x/H = 0.6$; and (d) effect of Sc_T at $x/H = 0.6$.

Furthermore, Table II shows that the memory requirements of the VIC is about 5% of the VIC-FDF.

The sensitivity of the velocity profiles in Figure 3 and the concentrations profiles in Figures 8, 9 and 15 to changes in grid number, in vortex blob number, and particles in Monte-Carlo technique has been investigated. The parameters used for the base run are chosen in such a way that the computational time was reasonable as shown in Table II. Grid number convergence was tested by reducing the grid by half, i.e. 128×128, keeping all other numerical parameters identical to the base run. Therefore the width and the length of the

Table II. Computational times and memory requirements for the 2D mixing layer.

Simulation	CPU time (min)	Memory (MB)
VIC	108	22
VIC-FDF (Smagorinsky)	5227	457
VIC-FDF (Dynamic)	5320	458

computational domain was reduced by half. The velocity and concentration profiles in the self-preserving region were insensitive to change in grid number. The sensitivity to change in the number of vortex blob was tested by doubling the number of vortex blobs from 2560 (for base run) to 5120, keeping the other numerical parameters identical to the base run. The profiles were insensitive to doubling the number of vortex blobs. Also, the sensitivity to change in the number of particles in the Monte-Carlo technique has been investigated by increasing the number of particles from $N_g = 36$ (base run) to $N_g = 49$. The results were insensitive to variation in N_g.

8. CONCLUDING REMARKS

A LES based on the diffusion-velocity method for the solution of the vorticity transport has been used in conjunction with the filtered density function to predict the flow field and scalar field of spatially growing mixing layer. The two-dimensional vortex-in-cell in conjunction with the Smagorinsky SGS model and dynamic eddy viscosity SGS model has been used to calculate the filtered flow field. The FDF transport equation has been solved using Lagrangian Monte-Carlo scheme.

The LES methodology based on vortex method results in the dynamic eddy viscosity SGS being less dissipative than the Smagorinsky SGS as found in previous works based on momentum equation. The dissipative effect of the SGS model was demonstrated by lower level of spanwise vorticity contours, lower cross-stream profiles of spanwise vorticity, lower cross-stream profiles for rms longitudinal and lateral velocity fluctuations as the eddy viscosity from SGS is higher. The self-similarity of rms longitudinal and lateral velocity fluctuations obtained using dynamic eddy viscosity SGS is better than the ones obtained using Smagorinsky SGS.

The mean and rms concentration fluctuations profiles in the self-preserving region are close to the results of previous numerical simulation and experiment. The mean concentration profiles exhibit triple inflection point. The scalar mixing region extends further into the free stream than does the momentum mixing region, indicating enhanced transport of scalar over momentum. The rms concentration profiles exhibit asymmetry and bimodal shape because high-speed fluid is mixing at a faster rate than low-speed fluid. The rms concentration profiles obtained using Smagorinsky SGS are lower than the ones obtained using dynamic eddy viscosity SGS because of increased mixing when Smagorinsky SGS is used. As the flow develops in the downstream direction, the FDFs develop from an initial U shape to FDFs exhibiting peaks biased toward the high-speed side with non-marching behaviour. This indicates that the mixing layer entrains and subsequently mixes larger quantities of high-speed fluid. The FDFs obtained using Smagorinsky SGS have peaks with higher probabilities and closer

to the mean value ($\zeta = 0.5$) than the ones obtained using dynamic eddy viscosity SGS. The mean concentration profiles, rms concentration fluctuations profiles and FDFs are sensitive to inflow boundary conditions with the combination of laminar boundary layer for flow field and error function for scalar field yielding profiles trends in agreement with previous experiment and simulation.

For the present mixing layer it is suggested that the VIC is advantageous over the finite difference because it is more robust and has less numerical diffusion keeping in mind that the computational requirements of VIC or finite-difference constitute a small percentage of the computational requirements of the VIC-FDF or finite difference-FDF, respectively.

Regarding the extension of the present 2D VIC to the physically more realistic 3D VIC, there are basically three differences. The first difference is that the velocity-vorticity formulation is used in 3D instead of stream function-vorticity formulation commonly used in 2D. The second difference is the additional stretching term in 3D, which is calculated on the grid and projected back to the particle as a source of vorticity [54], using an interpolation technique. The third difference is the extension of the diffusion velocity method to 3D which is problematic. A diffusion velocity vector for each component of vorticity appears in the vorticity transport. This may be numerically intractable unless the vector field $\Delta\boldsymbol{\omega}$ (Laplacian of vorticity) is decomposed into a vector parallel to $\boldsymbol{\omega}$ and a vector orthogonal to $\boldsymbol{\omega}$ [55]. This challenge is presently being undertaken.

ACKNOWLEDGEMENTS

This research was supported by a grant from the National Sciences and Engineering Research Council of Canada.

REFERENCES

1. Chorin AJ, Marsden JE. *A Mathematical Introduction to Fluid Mechanics*. Springer: Berlin, 1979.
2. Leonard A. Vortex methods for flow simulation. *Journal of Computational Physics* 1980; **37**:289–335.
3. Ghoniem AF, Givi P. Vortex-scalar element calculations of a diffusion flame stabilized on a plane mixing layer. *NASA Technical Memorandum 100133 ICOMP-87-4*, 1987.
4. Sarpkaya E. Vortex element methods for flow simulation. *Advances in Applied Mathematics* 1994; **31**:113–247.
5. Cottet GH, Koumoutsakos PD. *Vortex Methods*: *Theory and Practice*. Cambridge University Press: Cambridge, MA, 2000.
6. Ashurst WT. Numerical simulation of turbulent mixing layer via vortex dynamics. In *Turbulent Shear Flows I* vol. 1, Durst F *et al.* (eds). Springer: Berlin, 1979; 402–413.
7. Kuwahara K, Takami H. Study of turbulent wake behind bluff body by vortex method. *Proceedings of the IUTAM Symposium*. North-Holland Publishing Corporation: Amsterdam, 1983.
8. Ghoneim AF, Ng KK. Effect of harmonic modulation on rates of entrainment in a confined shear layer. *AIAA-86-0056*.
9. Inoue O, Leonard A. Vortex simulation of forced/unforced mixing layers. *AIAA Journal* 1987; **26**(11):1417.
10. Ghoniem AF, Ng KK. Numerical study of dynamics of a forced shear layer. *Physics of Fluids* 1987; **30**(3): 706–721.
11. Inoue O. Double-frequency forcing on spatially growing mixing layers. *Journal of Fluid Mechanics* 1992; **234**:553–581.
12. Aref H, Siggia ED. Vortex dynamics of the two-dimensional turbulent shear layer. *Journal of Fluid Mechanics* 1980; **100**:705–737.
13. Abdolhosseini R, Milane RE. On the effect of vortex grid density in the vortex-in-cell simulation of mixing layer. *International Journal for Computational Fluid Dynamics* 2000; **13**:161–183.
14. Mansfield JR, Knio OM, Meneveau C. A dynamic LES scheme for the vorticity transport equation: formulation and *a priori* tests. *Journal of Computational Physics* 1998; **145**:693–730.
15. Degond P, Mas-Gallic S. The weighted particle method for convection–diffusion equations. Part 1: the case of isotropic viscosity. *Mathematics of Computation* 1989; **53**(188):485–507.

16. Greengard C. The core spreading vortex method approximates the wrong equation. *Journal of Computational Physics* 1985; **61**:345–348.
17. Milane RE, Nourazar S. *Mechanics Research Communications* 1995; **22**(4):327–333.
18. Milane RE, Nourazar S. *Mechanical Research Communications* 1997; **24**(2):215–221.
19. Cottet GH. Artificial viscosity models for vortex and particle methods. *Journal of Computational Physics* 1996; **127**:299–308.
20. Ogami Y, Akamatsu T. Viscous flow simulation using the discrete vortex model—the diffusion velocity method. *Computers and Fluids* 1991; **19**(3/4):433–441.
21. Clarke NR, Tutty OR. Construction and validation of a discrete vortex method for the two-dimensional incompressible Navier–Stokes equations. *Computers and Fluids* 1994; **23**(6):751–783.
22. Milane RE. Large eddy simulation (2D) using diffusion-velocity method and vortex-in-cell. *International Journal for Numerical Methods in Fluids* 2004; **44**:837–860.
23. Ghoniem AF, Heidarinejad G. Effect of two-dimensional shear layer dynamics on mixing and combustion at low heat release. *Combustion Science and Technology* 1990; **72**:79–99.
24. Knio OM, Ghoniem AF. Three dimensional vortex simulation of rollup and entrainment in a shear layer. *Journal of Computational Physics* 1991; **79**:172–222.
25. Pope SB. A Monte Carlo method for the PDF equations of turbulent reactive flow. *Combustion Science and Technology* 1981; **25**:159–174.
26. Pope SB. PDF methods for turbulent reactive flows. *Progress in Energy and Combustion Science* 1985; **11**: 119–192.
27. Pope SB. *Turbulent Flows*. Cambridge University Press: Cambridge, MA, 2000.
28. Gao F, O'Brien EE. A large-eddy simulation scheme for turbulent reacting flows. *Physics of Fluids A* 1993; **5**(6):1282–1284.
29. Colucci PJ, Jaberi FA, Givi P, Pope SB. Filtered density function for large eddy simulation of turbulent reacting flows. *Physics of Fluids* 1998; **10**(2):499–515.
30. Jaberi FA, Colucci PJ, James S, Givi P, Pope SB. Filtered mass density function for large eddy simulation of turbulent flows. *Journal of Fluid Mechanics* 1999; **401**:85–121.
31. Zhou XY, Pereira JCF. Large eddy simulation (2D) of a reacting plane mixing layer using filtered density function. *Flow, Turbulence and Combustion* 2000; **64**:279–300.
32. Masutani SM, Bowman CT. The structure of a chemically reacting plane mixing layer. *Journal of Fluid Mechanics* 1986; **172**:93–126.
33. Konard JH. An experimental investigation of mixing in two-dimensional turbulent shear flows with applications to diffused-limited chemical reactions. *Ph.D. Thesis*, California Institute of Technology, 1977.
34. Batt RG. Turbulent mixing of passive and chemically reacting species in a low-speed shear layer. *Journal of Fluid Mechanics* 1977; **82**:53–89.
35. Pickett LM, Ghandhi JB. Passive scalar measurements in a planar mixing layer by PLIF of acetone. *Experiments in Fluids* 2001; **31**:309–318.
36. Clemens NT, Mungal MG. Large-scale structure and entrainment in the supersonic mixing layer. *Journal of Fluid Mechanics* 1995; **284**:171–216.
37. Zahrai S, Bark FH, Karlsson RI. On anisotropic subgrid modeling. *European Journal of Mechanics B-Fluids* 1995; **14**(4):459–486.
38. Sagaut P. Large eddy simulation for incompressible flows. *Scientific Computation*. Springer: Berlin, 2002.
39. Vreman B, Geurts B, Kuerten H. Large-eddy simulation of the turbulent mixing layer. *Journal of Fluid Mechanics* 1997; **339**:357–390.
40. Christiansen JP. Numerical solution of hydrodynamics by method of point vortices. *Journal of Computational Physics* 1973; **13**:363–379.
41. Baker GR. The cloud-in-cell technique applied to the roll-up of the vortex sheets. *Journal of Computational Physics* 1979; **31**:76–95.
42. Chorin AJ. Numerical study of slightly viscous flow. *Journal of Fluid Mechanics* 1973; **57**:785–796.
43. Oster D, Wygnanski I. The forced mixing layer between parallel streams. *Journal of Fluid Mechanics* 1982; **123**:91–130.
44. Pope SB. Lagrangian PDF methods for turbulent flows. *Annual Review of Fluid Mechanics* 1994; **26**:23–63.
45. Soteriou MC, Ghoneim AF. On the effects of the inlet boundary condition on the mixing and burning in reacting shear flows. *Combustion and Flame* 1998; **112**:404–417.
46. Spencer BW, Jones BG. Statistical investigation of pressure and velocity fields in turbulence two-stream mixing layer. *AIAA Fourth Fluid and Plasma Dynamic Conference*, 1971.
47. Deardoff J. A numerical study of three-dimensional turbulent channel flow at large Reynolds numbers. *Journal of Fluid Mechanics* 1970; **41**(2):463–480.
48. Shumann U. Subgrid scale model for finite difference simulations of turbulent flows in plane channels and annuli. *Journal of Computational Physics* 1975; **18**:376–404.
49. Kaltenbach H-J. Cell aspect ratio dependence of anisotropy measures for resolved and subgrid scale stresses. *Journal of Computational Physics* 1977; **136**:399–410.

50. Vanormelingen J, Van DBE. Scalar transport in plane mixing layers. *Heat and Mass Transfer* 1999; **35**(5): 383–390.
51. Launder BE. In *Heat and Mass Transport in Turbulence*, Bradshaw P (ed.). Springer: Berlin, 1976.
52. Bilger RW, Saetran LR, Krishnamoorthy LV. Reaction in a scalar mixing layer. *Journal of Fluid Mechanics* 1991; **233**:211–242.
53. Koochesfahani MM, Dimotakis PE. Mixing and chemical reactions in a turbulent liquid mixing layer. *Journal of Fluid Mechanics* 1986; **170**:83–112.
54. Doorly DJ, Liu CH. Vortex particle in cell method for three-dimensional unbounded flow computations. *International Journal for Numerical Methods in Fluids* 2000; **32**:29–50.
55. Huberson S, Rivoalen E, Hauville F. Simulation numérique des équations de Navier–Stokes 3D par une méthode particulaire. *Comptes Rendes de l Academie des Sciences Paris* 1997; **324**:543–549.

